OVERVIEW OF 6-X 6-FOOT WIND TUNNEL AERO-OPTICS TESTS

Donald A. Buell
Ames Research Center

SUMMARY

The paper describes the splitter-plate arrangement used in tests in the 6-x 6-Foot Wind Tunnel and how it was configured to study boundary layers, both heated and unheated, shear layers over a cavity, separated flows behind spoilers, accelerated flows around a turret, and a turret wake. The flows are characterized by examples of the steady-state pressures and of velocity profiles through the various types of flow layers. An introduction to the instrumentation used by other authors is included.

INTRODUCTION

A series of wind-tunnel tests was conducted as a cooperative program between NASA, the Air Force Weapons Laboratory, the Air Force Flight Dynamics Laboratory (AFFDL), and their contractors over a period of 4 years. The goal was to simulate flows representative of the airflow around an airplane, to measure the characteristics of optical wave propagation through the flow, to quantify the aerodynamic disturbances that distort the optical beam, and to confirm assumed relationships between aerodynamics and optics. The 6-x 6-Foot Wind Tunnel was selected because it permitted the use of models large enough to give a reasonable resolution with existing instrumentation. It also provided transonic flow, controllable Reynolds number, and less optical distortion than other Ames facilities.

This paper is an overview of the tests, with descriptions of the models and the steady-state flow characteristics of each model. In ensuing papers, Mr. Raman will describe the dynamic pressures which he measured in the flow and on the model surfaces; Capt. Wade Bailey will describe optical measurements that he and others from the Air Force Weapons Laboratory made by passing laser beams through the flows; Dr. Trollinger will describe his interferometry; Drs. William Rose and Dennis Johnson will describe the dynamic density characteristics inferred from their measurements with hot wires and a laser doppler velocimeter; and Dr. August Verhoff will compare optical degradations computed from the density characteristics with the degradations observed. The author is indebted to Mr. Raman for the boundary-layer profile data presented herein and to Maj. John Otten for his efforts in organizing and coordinating the test program. The basic model was

designed and built by McDonnell-Douglas Corporation under contract to the Air Force Weapons Laboratory. Later modifications were made in NASA shops at Ames Research Center.

Many of the tests (with pins, fences, and a cavity) have been reported in reference 1, and figures from that reference have been used where relevant. Later tests with a turret model have not been reported elsewhere and are described in somewhat more detail. The turret model was a small-scale replica of the "coelostat" model on which loads have been measured both at NASA and AFFDL. The "coelostat" loads data will be discussed in later papers on the large-scale aero-optics tests. This particular turret configuration was not selected because of its attributes but rather because of the availability of the model from AFFDL and the availability of comparison data.

SYMBOLS

C_p static-pressure coefficient, $\dfrac{\bar{p} - \bar{p}_\infty}{q}$

$\dot{m}$ mass flow of air injected into cavity, kg/sec

M free-stream Mach number at a station 97 cm downstream from the plate leading edge

M_L time-averaged local Mach number at arbitrary point in the flow

p static pressure at point of measurement, N/m^2

p_T total pressure at point of measurement, N/m^2

p_∞ free-stream static pressure where M is defined, N/m^2

p_{T_∞} free-stream total pressure where M is defined, N/m^2

q free-stream dynamic pressure, $1/2\rho_\infty V_\infty^2$, N/m^2

R free-stream Reynolds number per meter, $\dfrac{\rho_\infty V_\infty}{\mu_\infty}$

R_{EP} component parallel to splitter plate of distance from center of turret to external probe, cm

V_∞ free-stream velocity where M is defined, m/sec

x coordinate in downstream direction (figs. 2 and 6), cm

y coordinate in cross-stream direction parallel to plate (figs. 2 and 6), cm

z distance from surface of plate, cm

θ azimuth angle, when θ_{Cp} and θ_{EP} are equal, deg

θ_{CP} azimuth angle of turret cavity and cavity probe (fig. 7), deg

θ_{EP} azimuth angle between stream direction and R_{EP} (fig. 6), deg

μ_∞ free-stream viscosity where M is defined, kg/m-sec

ρ_∞ free-stream density where M is defined, kg/m^3

$(\bar{\ })$ time-averaged quantity

MODELS

Splitter Plate

Figure 1 shows the splitter plate used to isolate the modelled flows from the wind-tunnel boundary layer. The flows of interest were examined in the region between the return mirror and the plate. A window in the plate permitted laser beams to be passed through the pylon and the flow to the mirror and back to the instrumentation outside the wind tunnel.

In preliminary entries, the mirror was not used; instead, a splitter plate was attached to both wind-tunnel walls, and the beam was passed across the entire wind tunnel. However, it was found that the free-stream introduced enough unwanted disturbances to make the optical signal/noise ratio marginal, and the mirror was then added.

Pin/Fence/Cavity Models

Figure 2 is a view of the splitter plate from the center of the wind tunnel in two of many configurations. The figure also shows the probe supports for holding hot wires, pressures probes, etc. One of the supports was remotely adjustable in x and z, while the other was manually adjustable in 3 dimensions. The turbulence-generating pins were intended to thicken the boundary layer and improve the probing resolution. Other arrangements of pins were used in preliminary tests and are the subject of reference 2. The seeding pins were the means of adding particles to the flow to enhance the signal to a laser doppler velocimeter and were left in for most of the tests. Porous spoilers of various sizes and porosities could be attached ahead of the test volume. A cube-shaped cavity could also be installed in place of the window. A glass bottom in the cavity allowed a laser beam to be passed through the shear layer. It was also possible to change the front wall of the cavity to a porous wall for the purpose of injecting air into the cavity.

Cavity flow is an essential part of the simulation because it is often desirable to omit windows in the optical system being simulated. The power levels of projected high-energy lasers are such that window materials generally absorb enough energy to induce significant index of refraction variations. This, in turn, causes serious degradation in far-field intensity. Fences have proven to be an effective means of inhibiting cavity resonance. Hence, it was deemed useful to simulate the shear flows from cavities and fences, both separately and in combination. The various model configurations are described in table 1. Fence details are sketched in figures 3 and 4.

Heated Model

Figure 5 shows the splitter plate with a heated copper plate installed upstream of the test volume. It was possible to maintain the plate

temperature about 50°C above the total temperature of the wind tunnel to simulate a heat leak from an aircraft. However, the amount of energy added by this means was small relative to that in the nearby airstream, and only a few of the configurations were tested in combination with the heated plate.

Turret Model

Figures 6 and 7 show details of the turret and fairing mounted on the plate, and figure 8 is a photograph of the turret configuration. For these tests, the "external" probe support was made remotely adjustable in 3 directions, necessitating the opening of a large cavity in the downstream portion of the pylon. The fence is not intended to affect the flow around the turret, but only to protect the wiring in the pylon cavity. The turret azimuth could be controlled remotely, and a probe support in the turret was also remotely adjustable along an imaginary optical beam emanating from the turret cavity. It should be noted that no optical measurements were actually made with the turret configuration, except for interferometer studies by Dr. Trollinger. In order to cover the mechanism, the turret and fairing were mounted on a thin plate bolted on top of the aft 2/3 of the original splitter plate.

The fairing used in some of the tests with the turret was intended to reattach the flow downstream of the turret and to move the shock waves off of the turret surface. Coordinates of the fairing are given in table 2. A gap of about 0.16 cm existed between the fairing and turret.

INSTRUMENTATION

Optical measurements were under the direction of the Air Force Weapons Laboratory and consisted of sending laser beams of various wave lengths and diameters through the flow to detectors. Both line-spread function and modulation transfer function were evaluated with fast-scanning devices that minimized vibration interference.

Instruments for determining aerodynamic characteristics of the flows included hot wires, operated at both high and low over-heats, and pressure transducers, both dynamic and steady-state. These devices were operated in pairs or in greater multiples to obtain correlations from which scale lengths could be deduced and statistical averages could be determined. The pin, fence, and cavity flows were also probed with a laser-doppler velocimeter, which measured particle velocity, and with various forms of interferometry. Details of these measurements are reported elsewhere in this conference paper. Preliminary results from the hot wires and laser-doppler velocimeter have been reported in reference 3.

The flows were also probed with a multiple-tube total-pressure rake and by a 5-hole hemisphere-head directional probe similar to that described in reference 4. In addition, steady-state pressure taps and high-response pressure transducers were distributed about the plate and turret surfaces. All of the aerodynamic instrumentation except the directional probe are described in greater detail in reference 1.

The directional probe measured mean pressures at the intersection of the hemisphere surface with the axis of symmetry and on 4 equally-spaced rays from the center of the hemisphere and 45° from the axis. The probe was calibrated in a 5-cm jet at Mach numbers from 0.3 to 1.5 to give angle of attack, angle of sideslip, local Mach number, local total pressure, and derived parameters. The probe was recalibrated at zero flow angle in the 6-x 6-Foot Wind Tunnel. Figure 9 shows how the Mach number indicated by a ratio of pressures on the probe varies with true Mach number. Its sensitivity to such parameters as Mach number was limited but marginally usable at supersonic speeds. The calibration was checked at a high flow angle over the entire range of Mach numbers in the 6-x 6-Foot Wind Tunnel. The results are shown in figure 10. Errors are generally less than 5 percent except at M = 1.2. These results were obtained with curve fits of the parameter versus indicated flow angle and indicated Mach number. It is recognized that in the wake there would be an additional error of unknown magnitude due to fluctuation of the pressures being measured.

TESTS

The tests of the pin, fence, cavity, and heated plate models were performed in three wind-tunnel entries at free-stream Mach numbers from 0.6 to 0.9 and Reynolds numbers of 6.6 and 9.8 million/m (2 and 3 million/ft). Tests of the turret model in a separate entry were performed at free-stream Mach numbers from 0.62 to 1.49 at a Reynolds number of about 4.9 million/m (1.5 million/ft) and at Mach numbers from 0.62 to 0.95 at Reynolds numbers of 9.8 million/m (3 million/ft). For calibrations of the directional probe, the Mach number range was extended to 0.4 and 1.7 at the lower Reynolds number.

Model configurations 3 through 6 were investigated with a rake and surface static pressures only. Optical measurements were made on all other models except the turret. Selected models were chosen for an additional detailed probing of the flow, and these are indicated in table 1.

The total temperature of the wind tunnel varied from 290° to 305° K.

RESULTS

The results to be presented here consist only of steady-state pressures measured on the models, on the total-pressure rake, and on the directional probe. The presentation is intended to characterize the various flows simulated in the tests.

40

Plate Pressures

Figures 11 through 18 show pressure coefficients for the pin model, the fence model, and the cavity model with and without a small fence, for both high and low subsonic speeds. The data are taken from reference 1, which has additional data for these and other models. The test volume which was the object of both optical and aerodynamic probing lies between $x = 0$ and $x = 20$ cm.

The pressure data indicate a high speed flow over the pin area near the leading edge, a deceleration in front of the return mirror, some asymmetry in the tunnel flow as the plate pushed the air towards the opposite side, and a little asymmetry across the plate in the y direction, probably due to the concentration of the seeding pins at the center of the plate. None of these factors was thought to significantly detract from the objectives of the test. The fences are seen to cause considerable disturbance, and the cavity pressures indicate an appreciable gradient in the z direction. Reynolds number effects were typically negligible.

It should be noted here that the solid-wall cavity resonated in a depth mode at the low Mach number and in a fore-aft mode at the high Mach number. When the upstream cavity wall was made porous to permit air injection from a plenum next to the cavity wall, the acoustical absorption was sufficient to inhibit resonance even without air injection. The thick boundary layer approaching the cavity is thought to have also contributed to this result. Despite the dynamic air movement induced by the resonance, the steady-state pressures were not appreciably affected by the resonance, and the data of figures 15 and 16 are reasonably representative of either case.

Turret Pressures

Figures 19 through 23 present steady-state pressure coefficients over the turret and on the plate beside the turret. The turret cavity azimuth was 120°, at which angle the static-pressure taps in the turret were approximately streamwise. The figures show that there was little pressure recovery on the downstream side of the turret at high Mach numbers. Even the plate pressures in figures 20 and 22 indicate the presence of a sizable wake at a Mach number of 0.95. The main effect of the fairing appears to be increased velocities over and beside the turret except in the cutout region between the turret and fairing.

Boundary-Layer Profiles

Figures 24 through 26 show velocities calculated from pressure measurements in the pin, fence, and cavity boundary layers. One can see in figure 24 that the 2 cm boundary layer without pins was tripled in thickness by either the turbulence pins or seeding pins and that the combination (model 1) yielded a layer 8 cm thick. While not duplicating the profile of a naturally occurring boundary layer, this layer was thick and repeatable and was the subject of extensive measurements. Reference 1 shows that Mach number, Reynolds number, and fore-aft position had only minor effects on the profile. Figure 25 shows the large fence shear layer which proved to be detrimental to optical propagation. The mirror is seen to have negligible effect. Figure 26 shows profiles over the cavity which are little affected by resonance (model 14 to model 8) and are actually fairly close to the profiles of model 3, which also had seeding pins but no cavity. The effects of fence height and porosity are evident. Both model 13 and 14 were probed extensively.

Figures 27 and 28 show rake measurements upstream and downstream of the turret. Although no attempt was made to calculate velocities, it is apparent that the approaching boundary layer was similar to previous models without pins. Figure 28 indicates that the wake enlarged abruptly as Mach number was increased. Hot wire measurements in the wake have led to calculated values of optical degradation that were very large under some conditions.

A more relevant picture of the velocity distribution around the turret was given by measurements with the directional probe. This probe was positioned not only at different heights above the plate, but also at different radii from the center of the turret along the line of sight from the turret cavity. Figures 29 through 31 are representative of the magnitude and direction of the Mach number vector at one height above the plate. A large lateral spread of the wake is evident from these data at the higher Mach numbers.

Figures 32 through 35 show the absolute magnitude of the Mach number vectors at different heights above the plate. It is apparent that the wake at an azimuth angle of 150° and a Mach number of 0.95 was much larger than at the other conditions. Even the 90° azimuth position shows a disturbed region of accelerated flow at the higher Mach number which helps to make the higher Mach numbers a special problem in optical propagation. Mach number effects are summarized for one height in figures 36 and 37. The latter figures also illustrate the small Reynolds number effect. A similarly small effect of the fairing is shown in figures 38 and 39.

Figures 40 through 43 give local density data for conditions comparable to the Mach number data shown previously. Density gradients were again most troublesome at the higher Mach number. Both the local mean density and Mach number distributions are required to convert the hot wire readings to density fluctuations, as will be discussed in Dr. Rose's paper.

CONCLUDING REMARKS

This paper has described a series of models which created various flow disturbances in transonic wind-tunnel tests and provided a vehicle for exploring the relationship between aerodynamics and optical propagation. The paper has presented characterizations of the disturbed flows by means of steady-state pressure data and derived parameters measured on the surface, on a rake, and on a directional probe. The flows included thickened boundary layers, shear layers over a cavity and behind porous spoilers, accelerated flow around a turret, and a turret wake. Detailed optical and aerodynamic measurements made in the flows are presented in subsequent papers.

REFERENCES

1. Buell, Donald A.: Aerodynamic Properties of a Flat Plate With Cavity for Optical-Propagation Studies. NASA TM-78487, January 1979.

2. Otten, L. J.; and Van Kuren, J. T.: Artificial Thickening of Transonic Boundary Layers. AIAA Paper 76-51, 1976.

3. Johnson, D. A.; and Rose, W. C.: Turbulence Measurements in a Transonic Boundary Layer and Free-Shear Flow Using Laser Velocimetry and Hot-Wire Anemometry Techniques. AIAA Paper 76-399, July 1976.

4. Armistead, Katharine H.; and Webb, Lannie, D.: Flight Calibration Tests of a Nose-Boom-Mounted Fixed Hemispherical Flow-Direction Sensor. NASA TN D-7461, October 1973.

TABLE 1.- MODEL CONFIGURATIONS

No.	Seed pins	Turbulence-generating pins	Return mirror	Fence height, cm	Fence porosity	Fence hole diameter, cm	Cavity	Cavity wall porosity	Cavity wall hole diameter, cm	Step height cm	Probe measurement
1	X	X	X	–	–	–	–	–	–	–	X
2	X	–	X	5.1	0.49	0.37	–	–	–	–	X
3	X	–	X	–	–	–	–	–	–	–	–
4	X	–	–	–	–	–	–	–	–	–	–
5	X	–	–	5.1	0.49	0.37	–	–	–	–	–
6	X	X	–	–	–	–	–	–	–	–	–
7	X	–	X	5.1	0.53	0.95	–	–	–	–	–
8	X	–	X	–	–	–	X	0	–	–	X
9	X	–	X	2.3	0.38	0.24 slits	X	0	–	–	–
10	X	–	X	2.3	0.38	0.52	X	0	–	–	–
11	X	–	X	4.6	0.38	0.52	X	0	–	–	X
12	X	–	X	4.6	0.58	0.99	X	0	–	–	–
13	X	–	X	2.3	0.58	0.99	X	0	–	–	X
14	X	–	X	–	–	–	X	0.49(Upst)	0.32	–	X
15	X	–	X	–	–	–	X	–	0.64slot	–	–
16	X	–	X	2.3	0.58	0.99	X	0.49(Upst)	0.32	–	–
18	–	–	X	–	–	–	–	–	–	0.64	–
19	–	–	X	–	–	–	–	–	–	–	–
20	–	X	X	–	–	–	–	–	–	–	–
21	–	X	X	–	–	–	–	–	–	0.64	–
Turret	–	–	–	4.6*	0.58*	0.99*	Fig.7	0.35	0.16	–	X

* Fence downstream of turret

TABLE 2.- TURRET - FAIRING COORDINATES

x, cm	Upper Surface		Lower Surface	
	y, cm	z, cm	y, cm	z, cm
-0.23	0.00	4.65		
0.00	0.00	4.83	0.00	4.52
0.00	0.23	4.75		
0.00	0.36	4.52		
1.37	0.00	5.00	0.00	4.39
1.37	0.28	4.98		
1.37	0.56	4.83		
1.37	0.69	4.37		
3.56	0.00	5.08	0.00	3.51
3.56	0.28	5.05	0.48	3.48
3.56	0.56	5.00	0.94	3.40
3.56	0.84	4.85		
3.56	1.07	4.67		
3.56	1.27	4.39		
3.56	1.35	4.11		
3.56	1.37	3.84		
3.56	1.35	3.56		
3.56	1.35	3.38		
4.67	0.00	5.03	0.00	2.57
4.67	0.28	5.00	0.41	2.54
4.67	0.56	4.98	0.79	2.49
4.67	0.84	4.91	1.17	2.41
4.67	1.12	4.80	1.55	2.29
4.67	1.42	4.65		
4.67	1.70	4.37		
4.67	1.80	4.11		
4.67	1.88	3.84		
4.67	1.91	3.56		
4.67	1.91	3.28		
4.67	1.85	3.00		
4.67	1.80	2.72		
4.67	1.80	2.44		
5.82	0.00	4.93	0.00	0.99
5.82	0.28	4.93	0.25	0.99
5.82	0.56	4.88	0.51	0.97
5.82	0.84	4.83	0.76	0.89
5.82	1.12	4.72	1.02	0.81
5.82	1.42	4.60	1.27	0.71
5.82	1.70	4.42	1.50	0.61
5.82	1.98	4.19	1.70	0.46
5.82	2.23	3.84	1.91	0.30
5.82	2.39	3.56		
5.82	2.46	3.28		
5.82	2.51	3.00		
5.82	2.54	2.72		
5.82	2.67	2.13		
5.82	2.82	1.85		
5.82	2.97	1.57		
5.82	3.15	1.30		
5.82	3.33	1.02		

TABLE 2.- Continued

Upper Surface

x, cm	y, cm	z, cm
5.82(cont.)	3.56	0.74
5.82	3.81	0.46
5.82	4.19	0.00
6.93	0.00	4.80
6.93	0.28	4.80
6.93	0.56	4.75
6.93	0.84	4.70
6.93	1.12	4.62
6.93	1.42	4.50
6.93	1.70	4.39
6.93	1.98	4.24
6.93	2.26	4.04
6.93	2.46	3.84
6.93	2.69	3.56
6.93	2.84	3.28
6.93	2.97	3.00
6.93	3.05	2.72
6.93	3.15	2.44
6.93	3.28	2.13
6.93	3.43	1.85
6.93	3.61	1.57
6.93	3.78	1.30
6.93	4.01	1.02
6.93	4.24	0.74
6.93	4.52	0.41
6.93	4.88	0.00
8.08	0.00	4.65
8.08	0.56	4.57
8.08	1.12	4.42
8.08	1.70	4.22
8.08	2.26	3.89
8.08	2.82	3.43
8.08	3.38	2.79
8.08	3.96	1.88
8.08	4.52	0.99
8.08	5.08	0.30
8.08	5.21	0.00
10.90	0.00	4.17
10.90	0.53	4.14
10.90	1.09	4.01
10.90	1.63	3.81
10.90	2.18	3.53
10.90	2.72	3.12
10.90	3.28	2.67
10.90	3.81	1.72
10.90	4.34	0.91
10.90	4.90	0.28
10.90	5.16	0.00

Upper Surface

x, cm	y, cm	z, cm
13.72	0.00	3.61
13.72	0.51	3.56
13.72	1.02	3.48
13.72	1.55	3.33
13.72	2.06	3.07
13.72	2.57	2.72
13.72	3.07	2.21
13.72	3.58	1.52
13.72	4.09	0.81
13.72	4.62	0.23
13.72	4.83	0.00
16.54	0.00	3.02
16.54	0.43	3.00
16.54	0.94	2.90
16.54	1.40	2.77
16.54	1.85	2.57
16.54	2.34	2.26
16.54	2.79	1.85
16.54	3.25	1.27
16.54	3.73	0.69
16.54	4.34	0.00
19.35	0.00	2.41
19.35	0.41	2.39
19.35	0.82	2.31
19.35	1.22	2.21
19.35	1.63	2.03
19.35	2.01	1.80
19.35	2.41	1.50
19.35	2.82	1.04
19.35	3.23	0.58
19.35	3.73	0.00
22.17	0.00	1.65
22.17	0.33	1.63
22.17	0.66	1.60
22.17	0.99	1.50
22.17	1.27	1.40
22.17	1.63	1.24
22.17	1.96	1.04
22.17	2.29	0.74
22.17	2.62	0.41
22.17	3.00	0.00
24.99	0.00	0.79
24.99	0.43	0.76
24.99	0.86	0.69
24.99	1.27	0.53
24.99	1.70	0.28
24.99	2.18	0.00
27.33	0.00	0.00

Figure 1.- Three-view drawing of the splitter plate with return mirror.

LINEAR DIMENSIONS IN cm

TURB.-GEN. PINS, 0.32 D
HEIGHT: UPST., 4.8; DWNST., 3.5

FENCE

48.3 10.2

FIXED PROBE

SUPPORT STRUT
HEIGHT = 7.0 TO 17.1

3.2

3.8 (TYP.)

NON-CAVITY
CONFIGURATIONS

+Y

MOVABLE PROBE

1.9

22.9

17.3

WINDOW

113.2

135.7

+X

FENCE

25.4 15.2 3.3 (TYP.)

2.5
(TYP.)

CAVITY
CONFIGURATIONS

+Y

11.4

CAVITY, 15.2 DEEP

135.3

139.7

15.2

+X

SEEDING PINS, 0.32 D
HEIGHT = 5.1

LINEAR DIMENSIONS IN cm

Figure 2.- Top views of the pin, fence, and cavity models (return mirror removed).

LENGTH = 48.3 (TYP., BOTH FENCES)

0.32

0.32 (TYP.)

0.32 (TYP.)

0.32

MODEL

0.32 (TYP.)

0.32 (TYP.)

5.1

1133 HOLES, POROSITY = 0.49

2

0.37 D

0.81

0.91 (TYP.)

0.91 (TYP.)

0.64

5.1

0.64 (TYP.)

0.64 (TYP.)

182 HOLES, POROSITY = 0.53

7

0.95 D

LINEAR DIMENSIONS IN cm

Figure 3.- Sketch of the no-cavity fences; thickness = 0.46 cm.

50

LENGTH = 25.4 (TYP. ALL FENCES)

MODEL

46 SLOTS, POROSITY = 0.38   9

105 HOLES, POROSITY = 0.38   10

210 HOLES, POROSITY = 0.38   11

88 HOLES, POROSITY = 0.58   12

44 HOLES, POROSITY = 0.58   13, 16

LINEAR DIMENSIONS IN cm
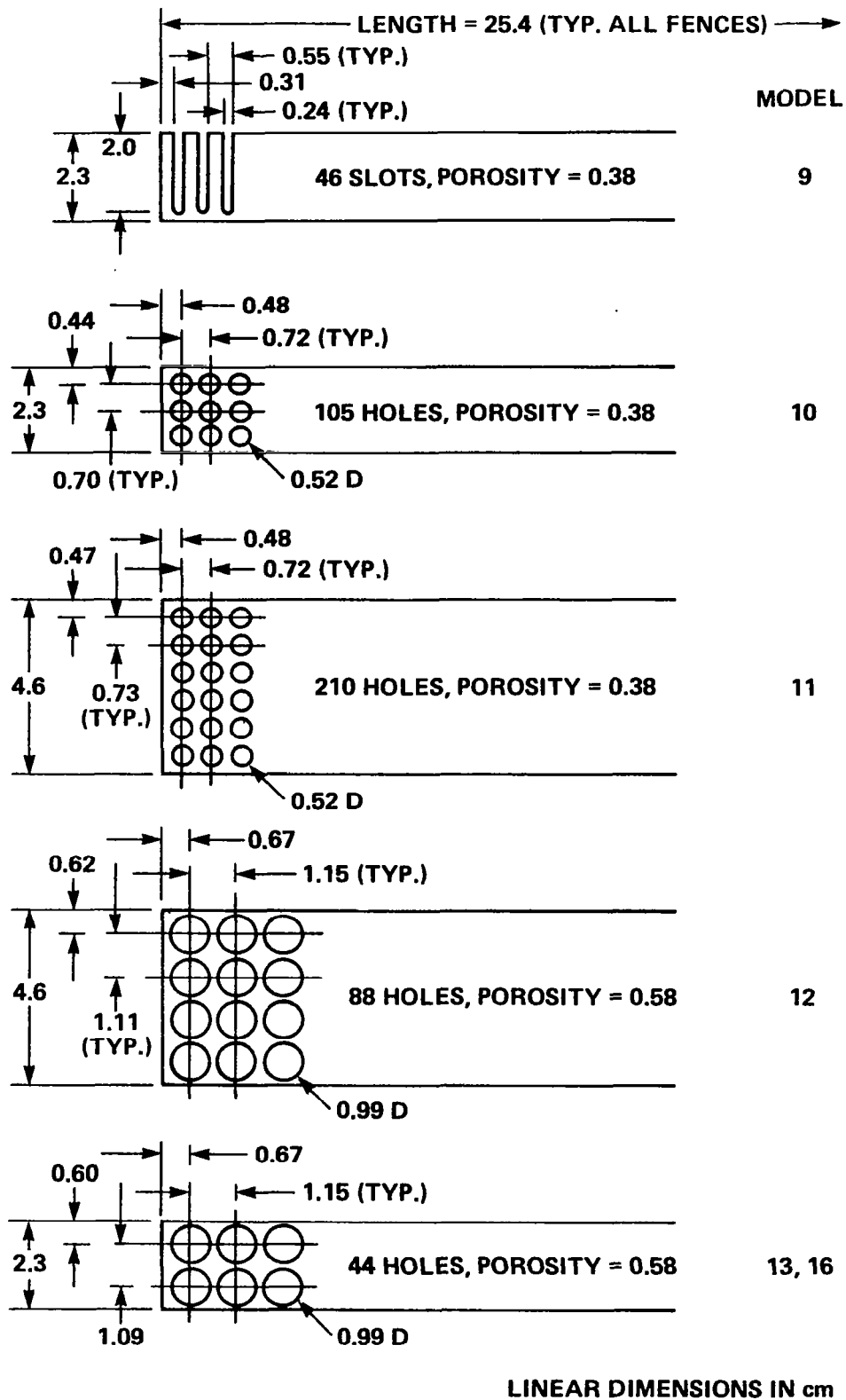
Figure 4.- Sketch of the cavity fences; thickness = 0.48 cm.

48.3 — 25.4

69.3
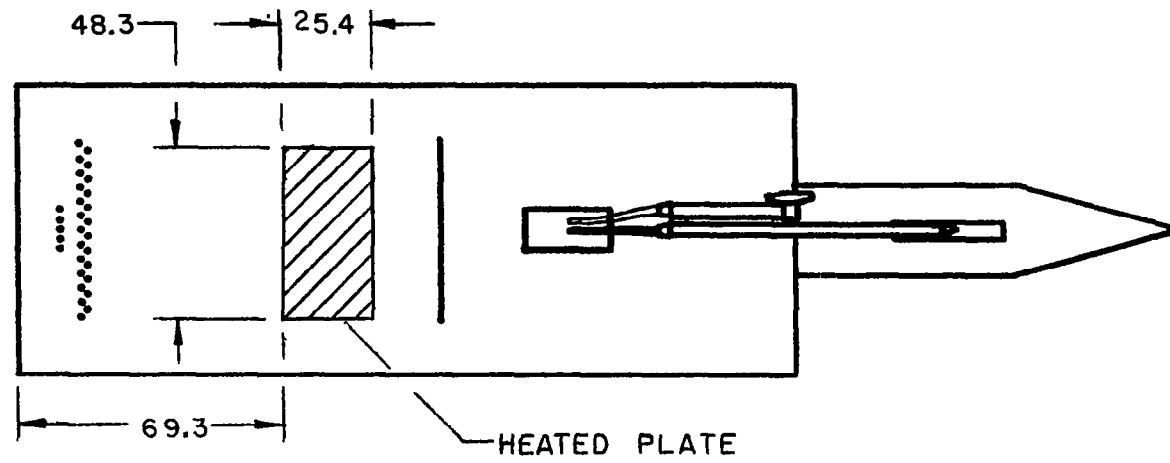
HEATED PLATE

LINEAR DIMENSIONS IN cm

Figure 5.- Top view of the heated-plate model (return mirror removed).

208.3

TURRET

FAIRING

61.6 86.0

76.2

3.2

FENCE FROM MODEL 12

38.1

R_{EP}

+Y

Θ_{EP}

EXTERNAL PROBE

PRESSURE TAP

54.3

+X

LINEAR DIMENSIONS IN cm

+Z

2.5 1.3
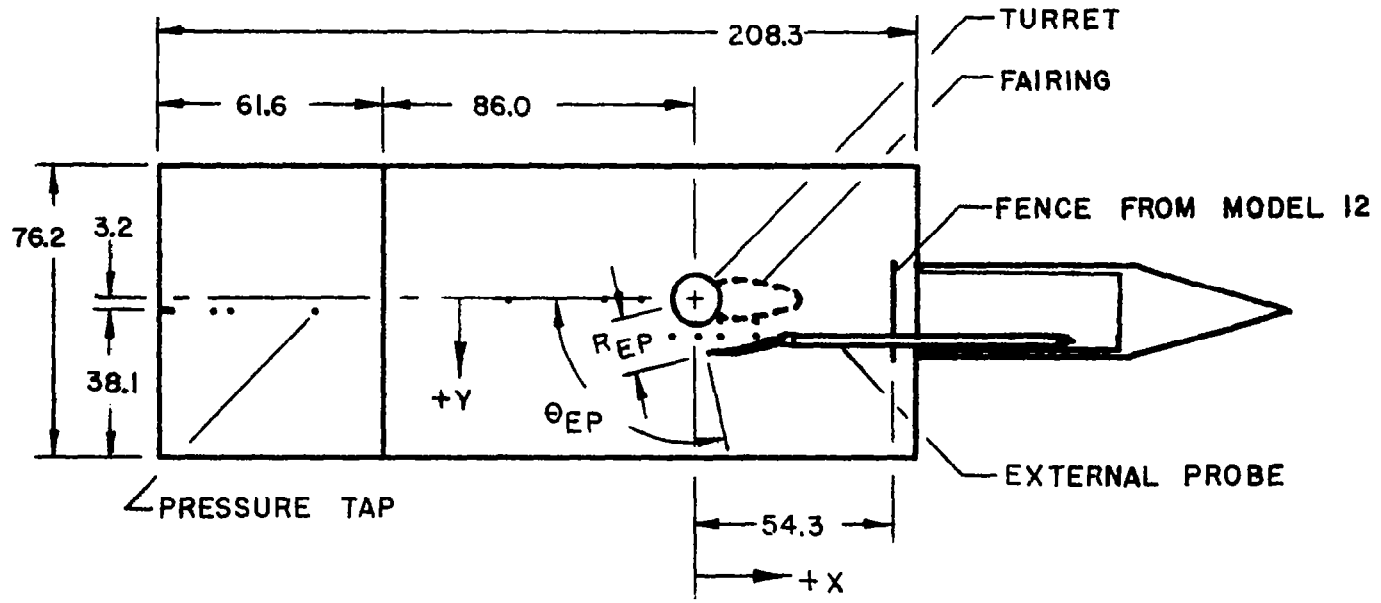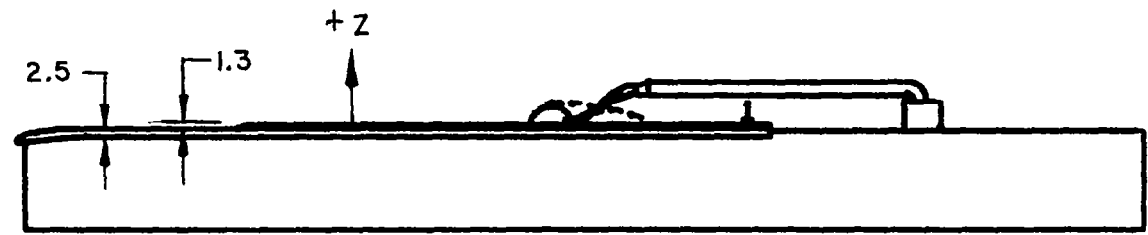
Figure 6.- Top and side views of the turret model.

12.1

10.4

θ_{cp}

27.3

2.9 O.D., 2.5 I.D.

6.4 SPHERICAL RADIUS

A

LINEAR DIMENSIONS IN cm

POROUS TUBE

1.7

0.2

4.4

2.0

A

CAVITY PROBE
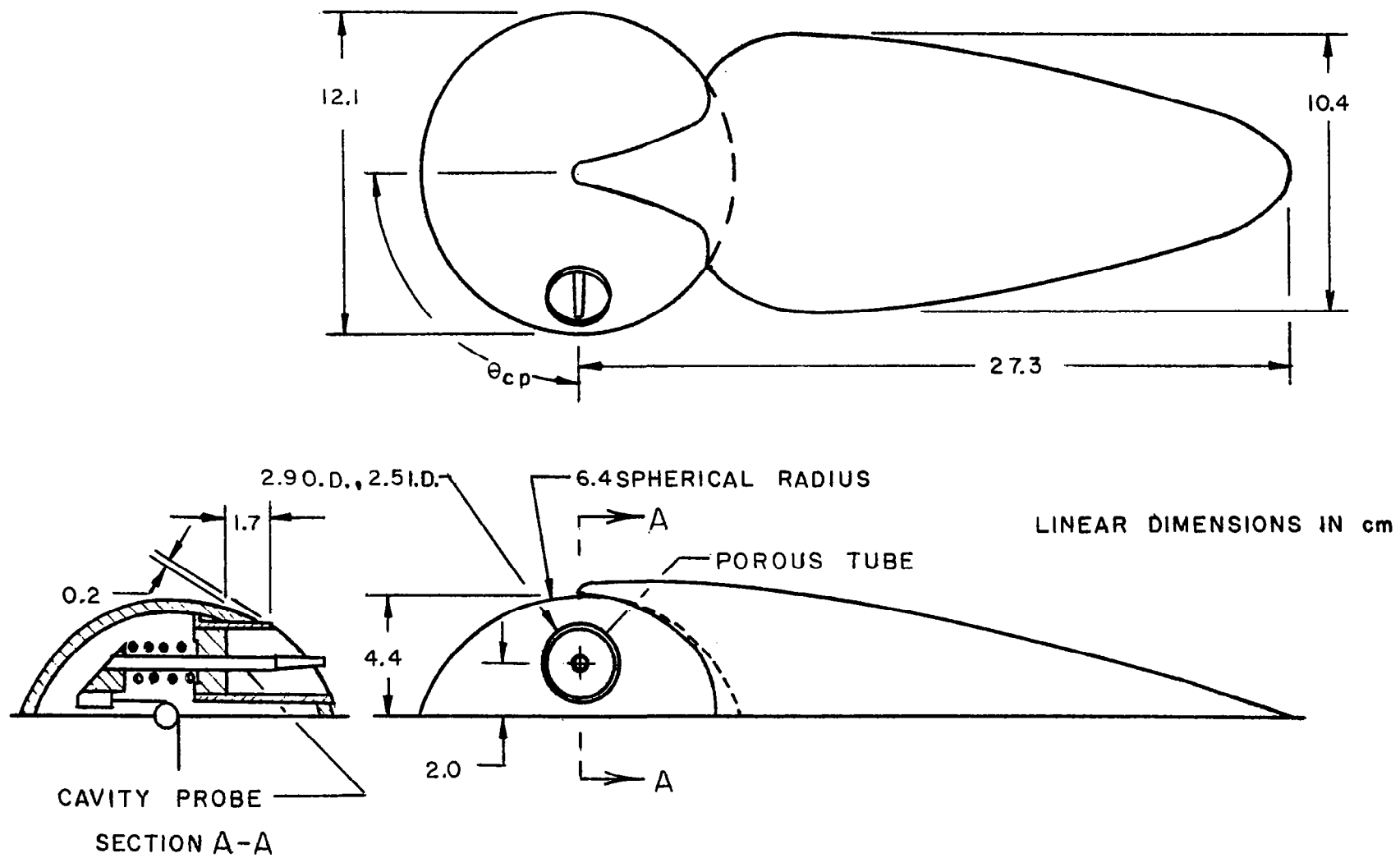
SECTION A-A

Figure 7.- Dimensions of the turret and fairing.
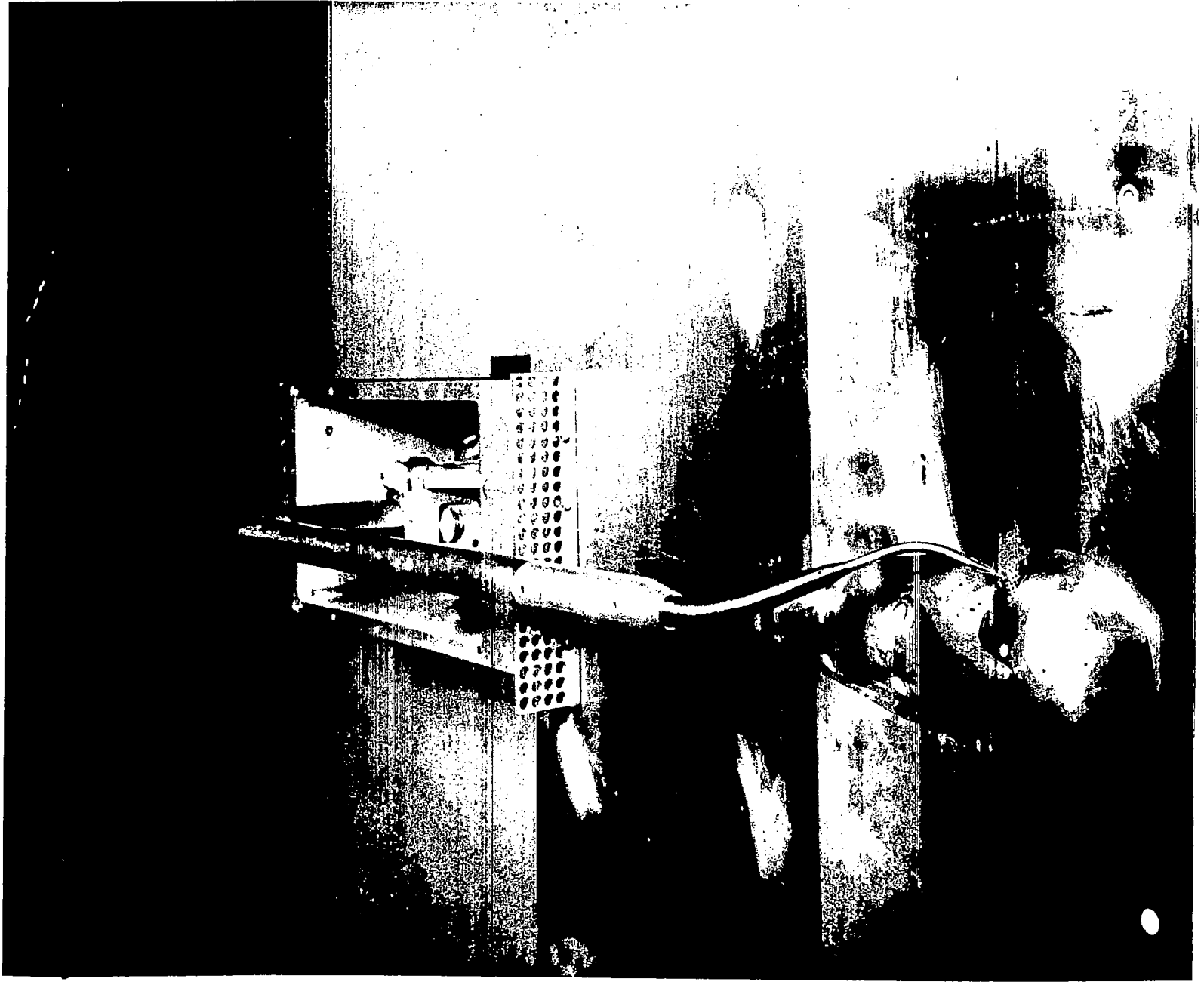
Figure 8.- Photograph of the turret and fairing with the external probe.
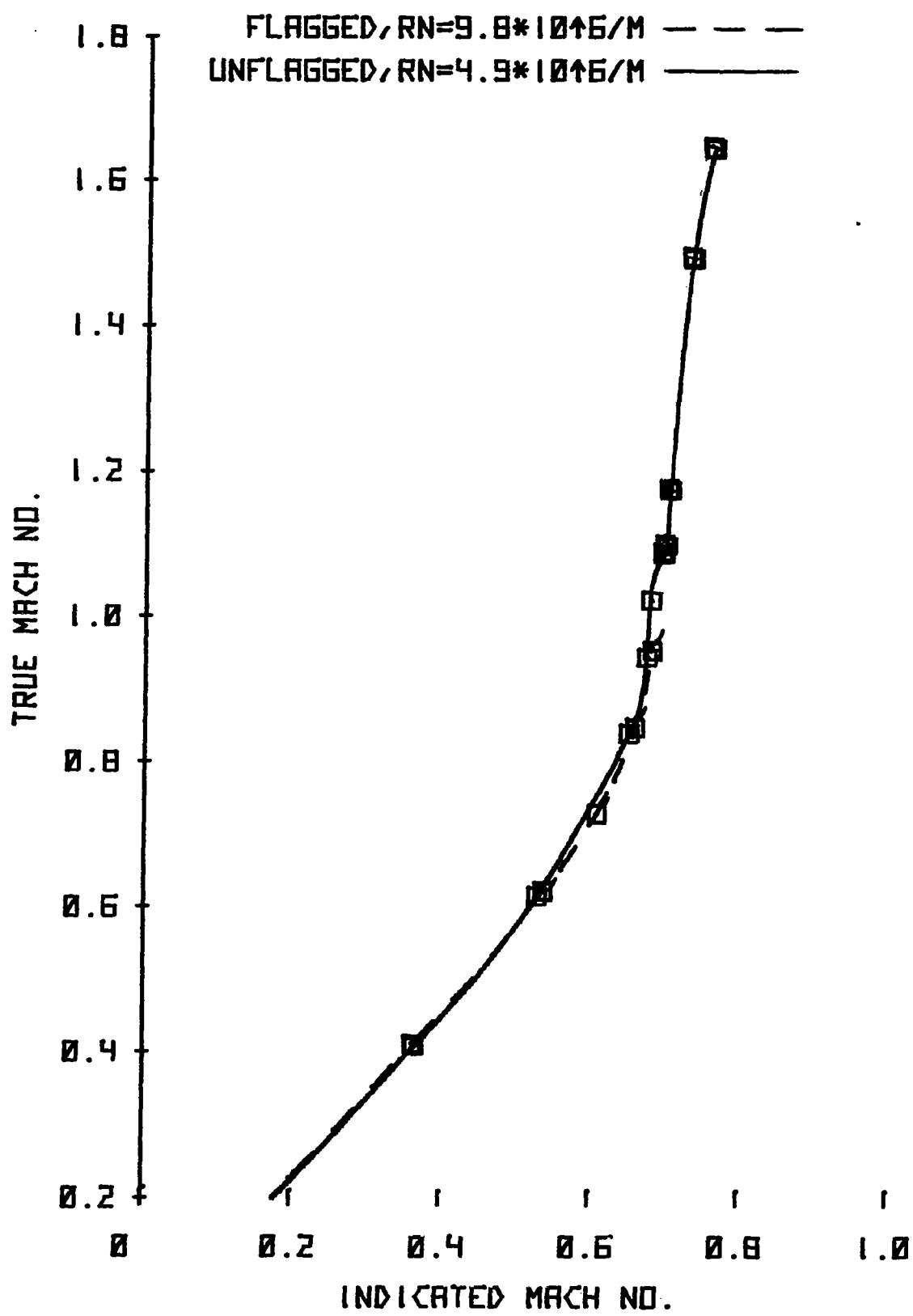
Figure 9.- Mach number calibration of the directional probe.
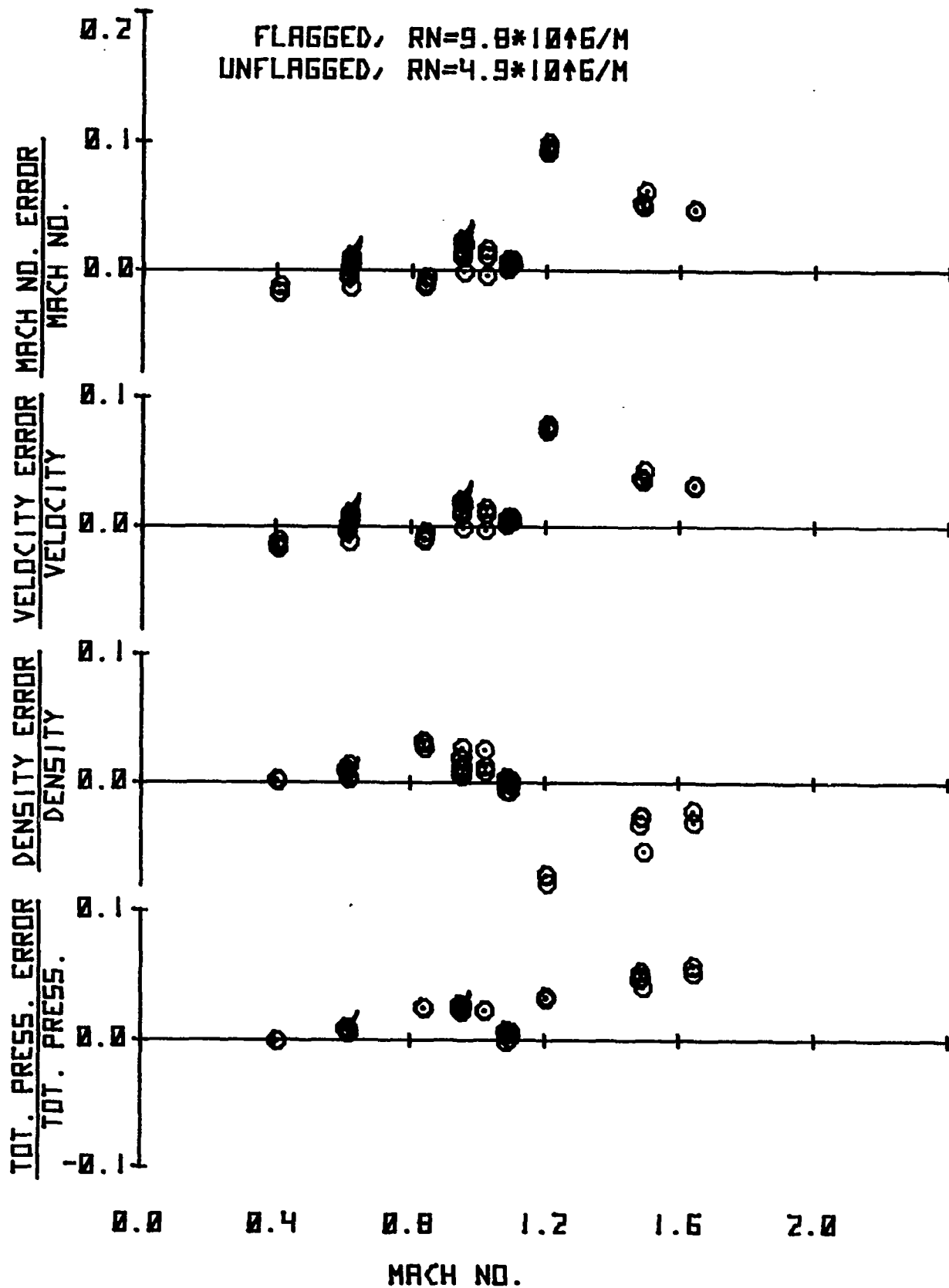
Figure 10.- Calibration errors of the directional probe at large flow angles; angle of attack = 8°, angle of sideslip = 28°.
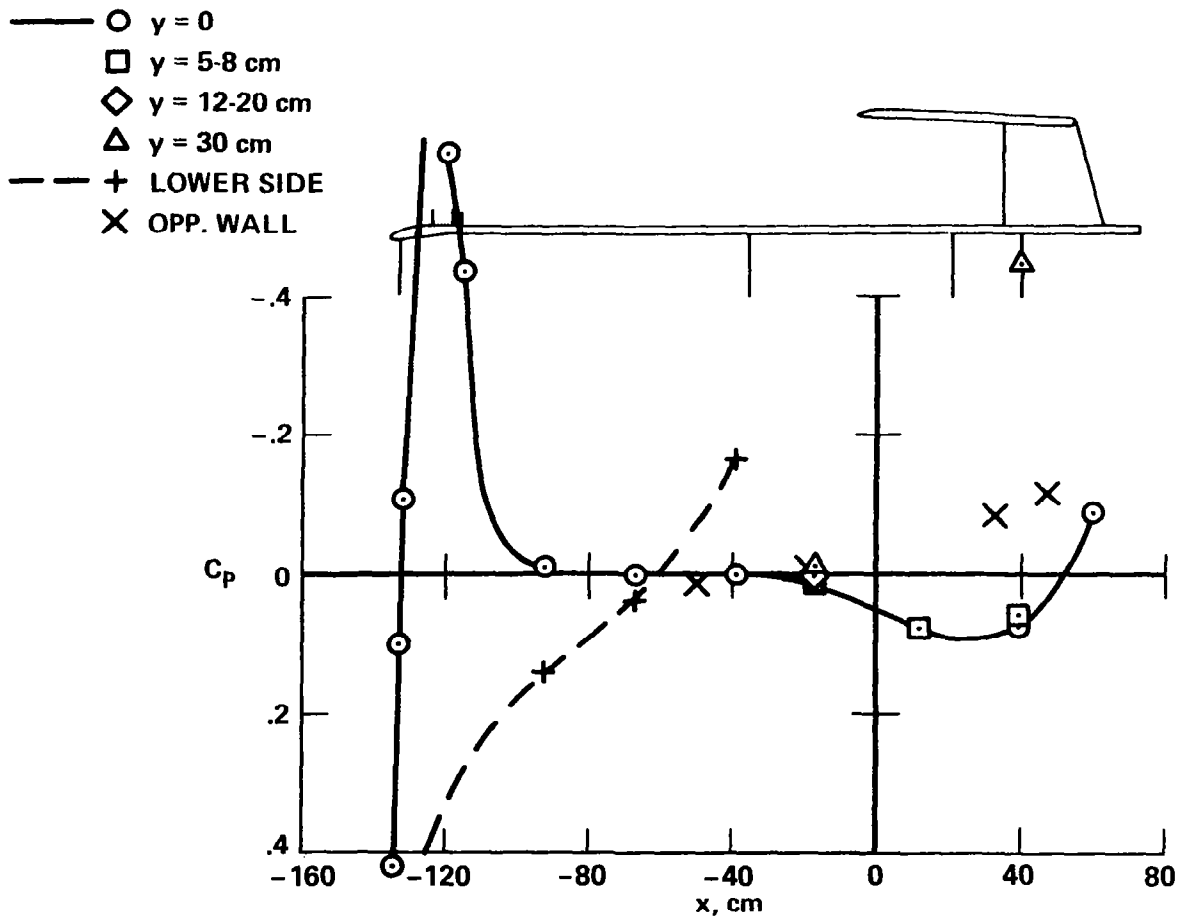
Figure 11.- Static-pressure coefficients on the plate and wall; pin model 1, M = 0.89, R = 9.8 million/m.
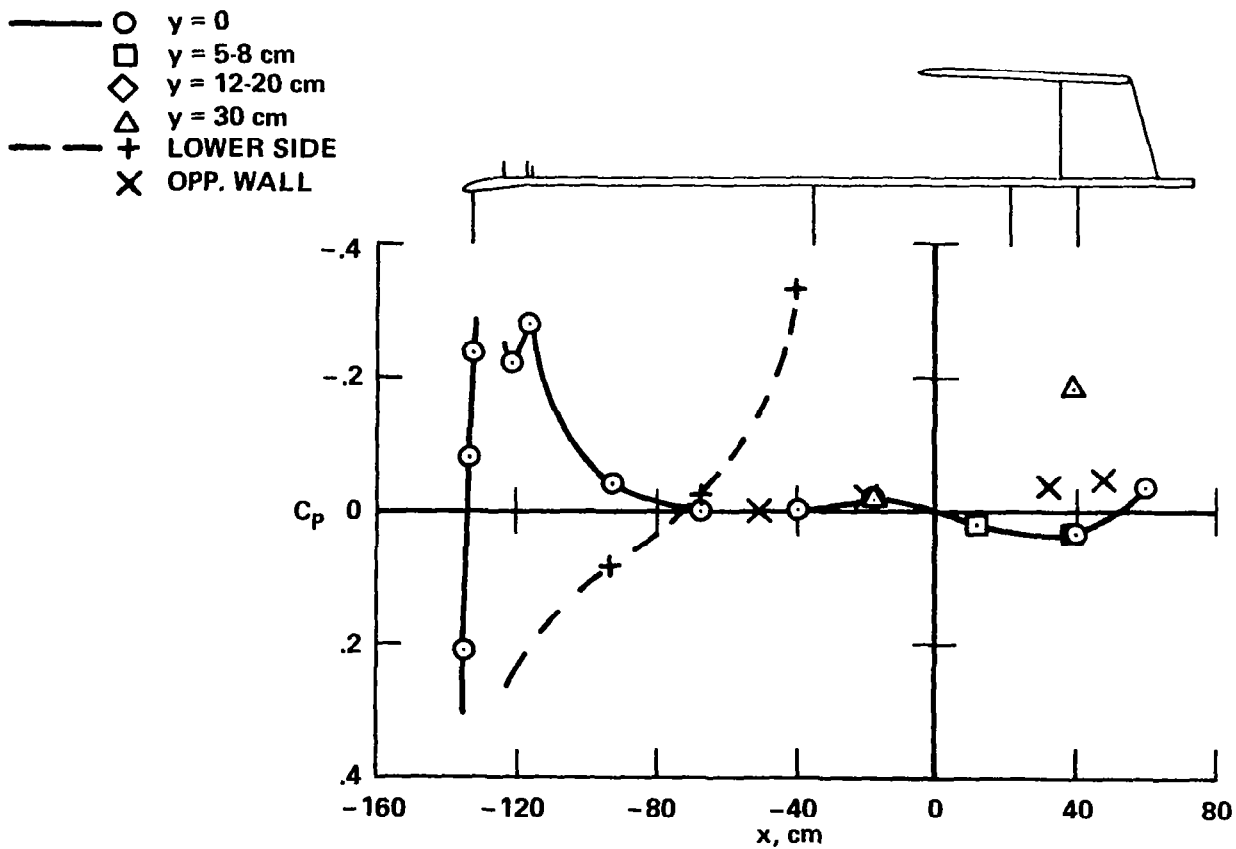
Figure 12.- Static-pressure coefficients on the plate and wall; pin model 1, M = 0.60, R = 9.8 million/m.
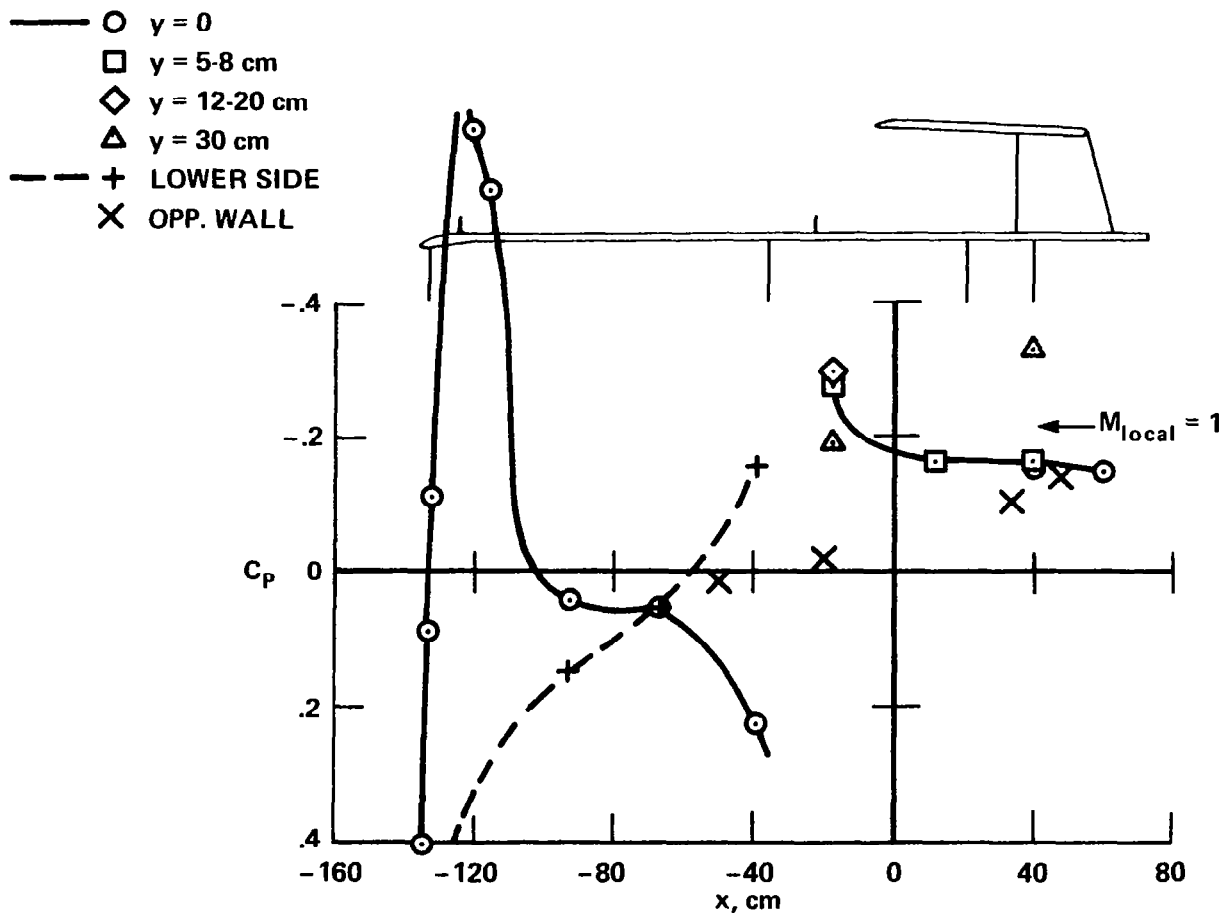
Figure 13.- Static-pressure coefficients on the plate and wall; fence model 2, M = 0.89, R = 9.8 million/m.
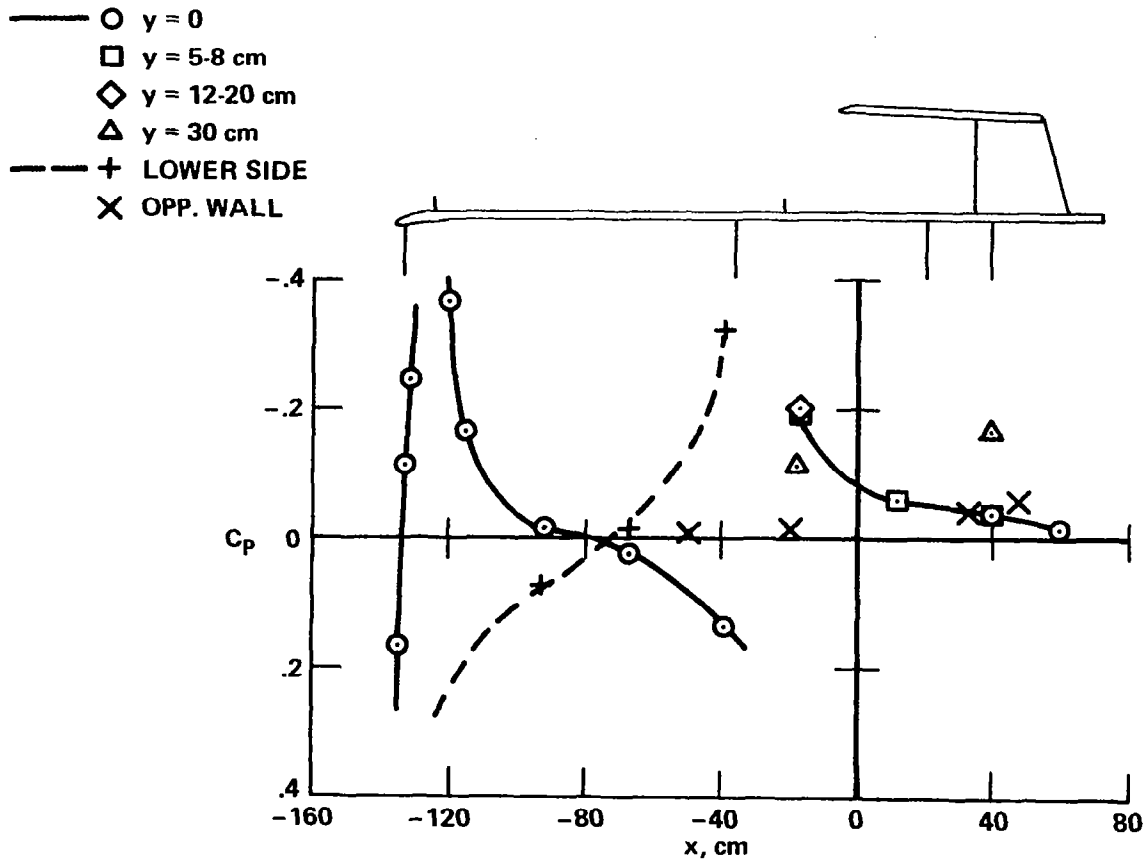
Figure 14.- Static-pressure coefficients on the plate and wall; fence model 2, M = 0.60, R = 9.8 million/m.
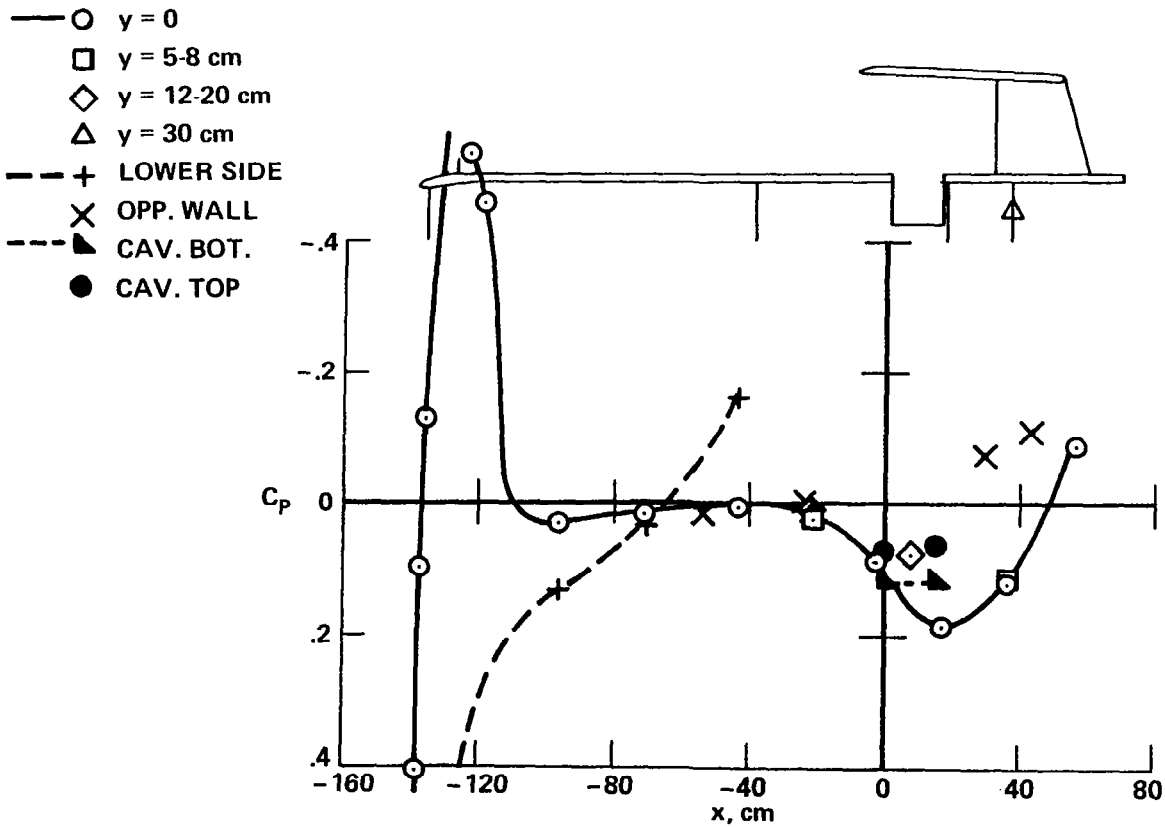
Figure 15.- Static-pressure coefficients on the plate, wall, and cavity; solid-wall cavity model 8, M = 0.89, R = 9.8 million/m.
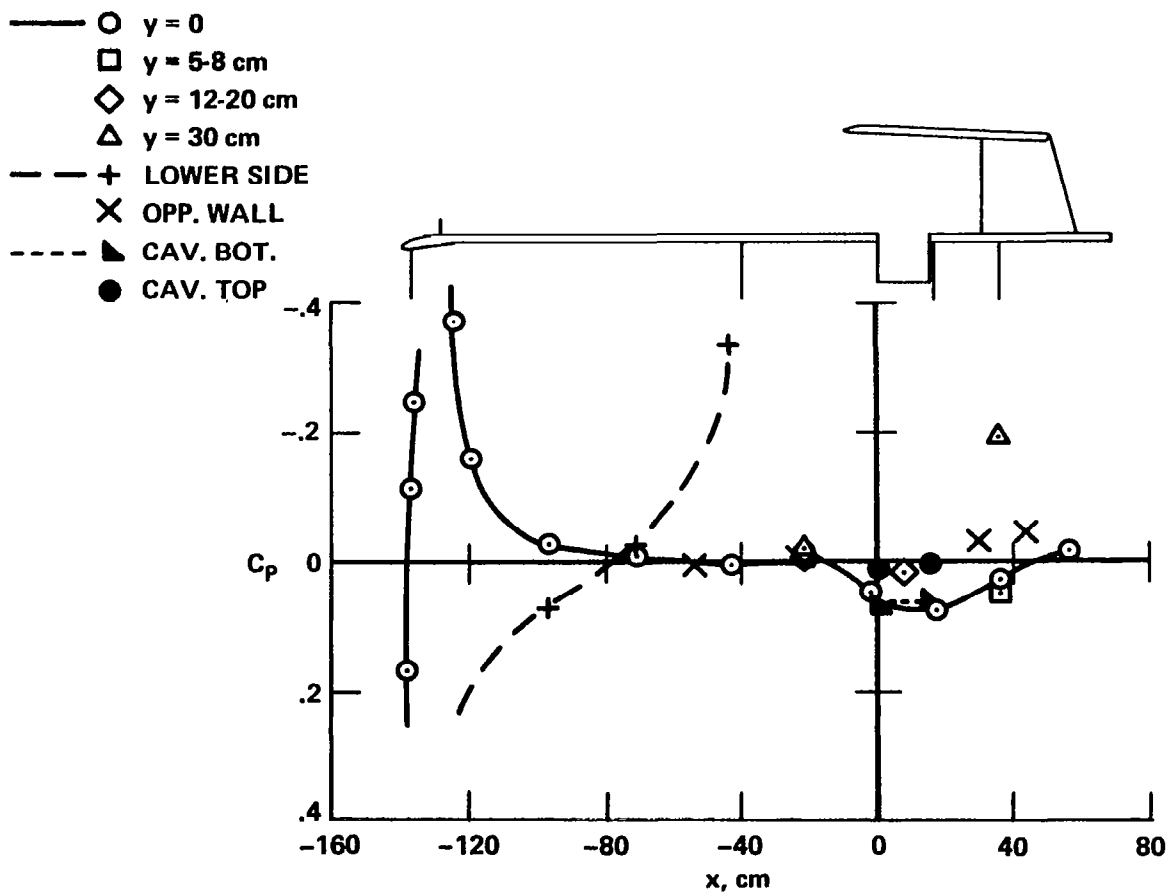
Figure 16.- Static-pressure coefficients on the plate, wall, and cavity; solid-wall cavity model 8, M = 0.60, R = 9.8 million/m.
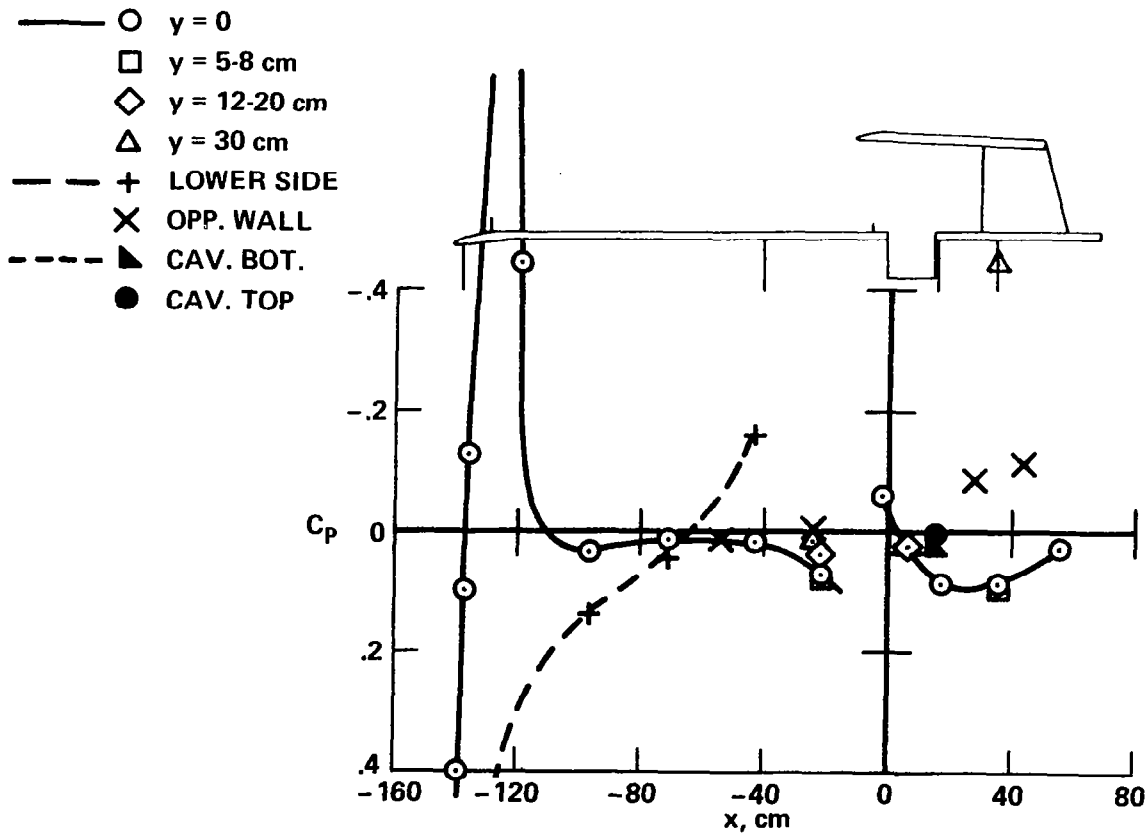
Figure 17.- Static-pressure coefficients on the plate, wall, and cavity; fence-cavity model 13, M = 0.89, R = 9.8 million/m.
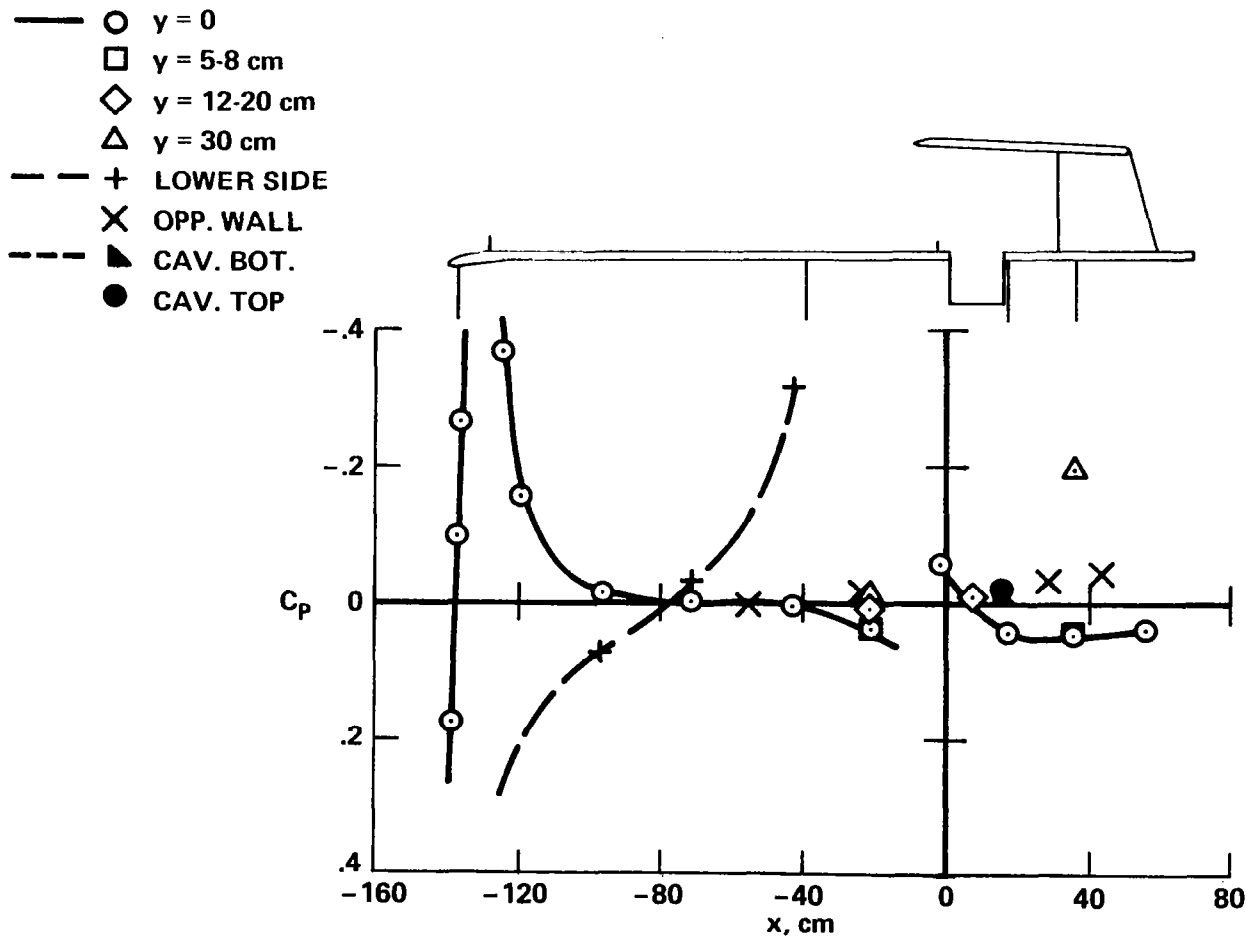
Figure 18.- Static-pressure coefficients on the plate, wall, and cavity; fence-cavity model 13, M = 0.60, R = 9.9 million/m.
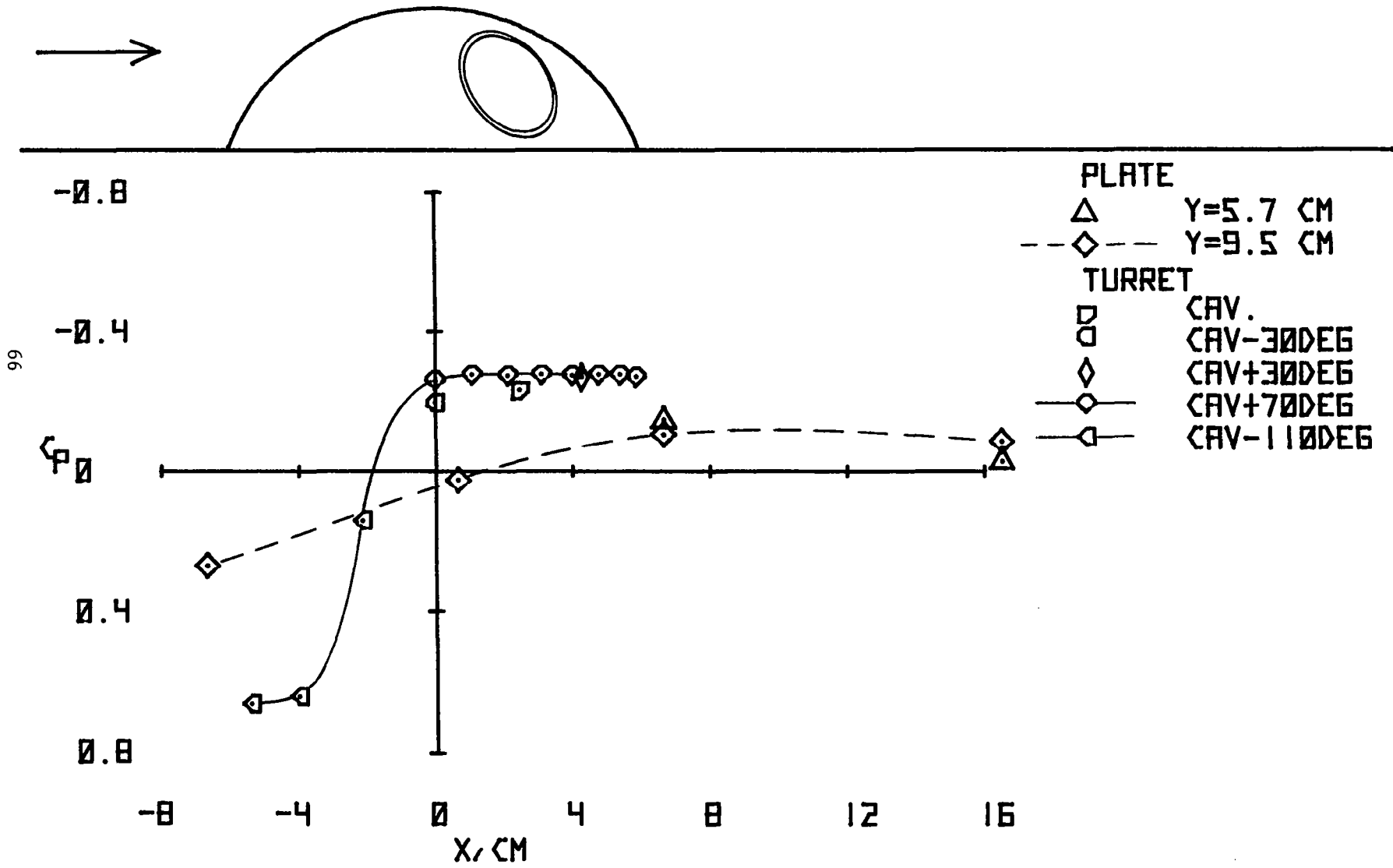
Figure 19.- Static-pressure coefficients on the turret and plate; M = 1.49, R = 4.8 million/m, θ = 120°.
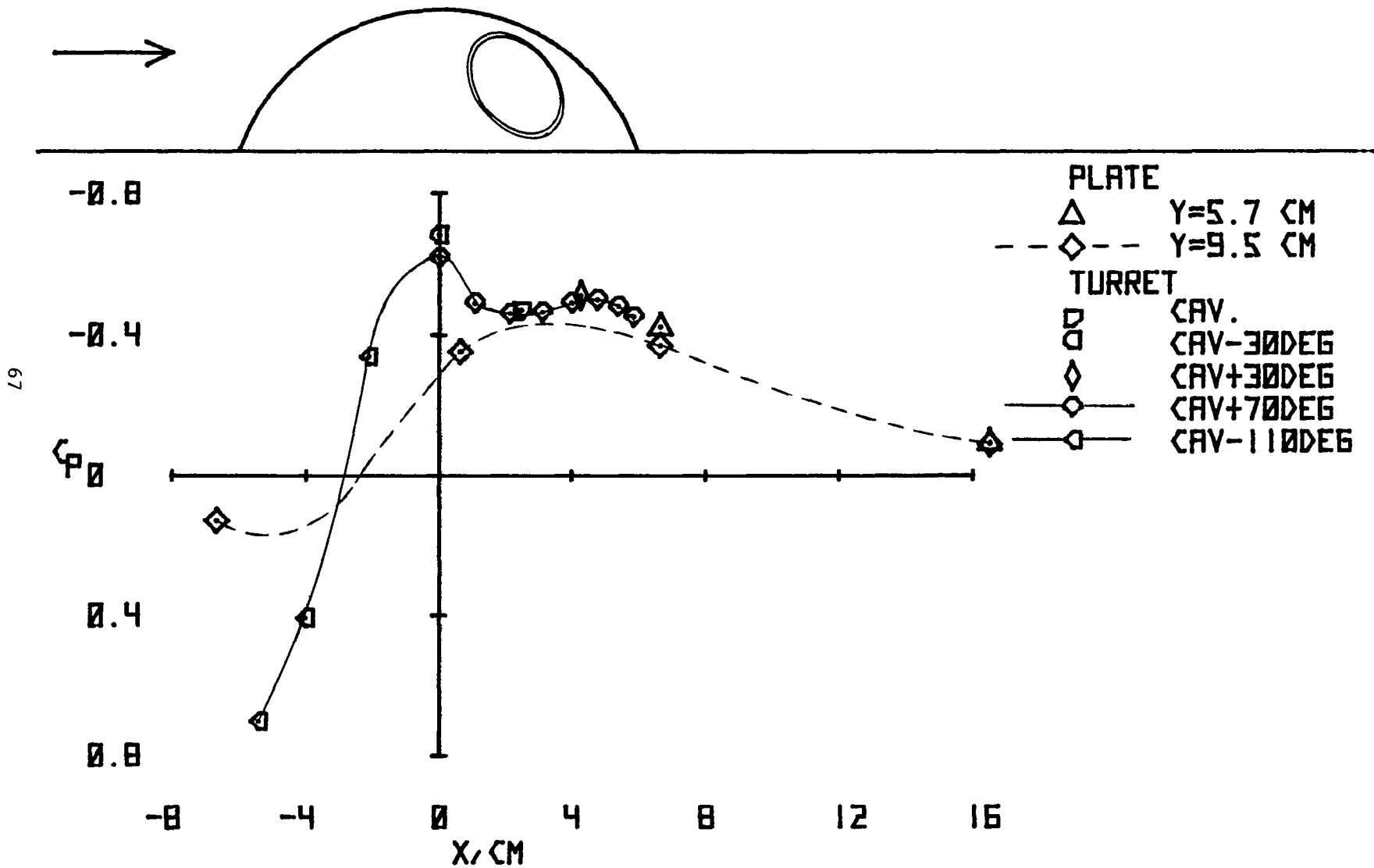
Figure 20.- Static-pressure coefficients on the turret and plate; M = 0.95, R = 4.9 million/m, θ = 120°.
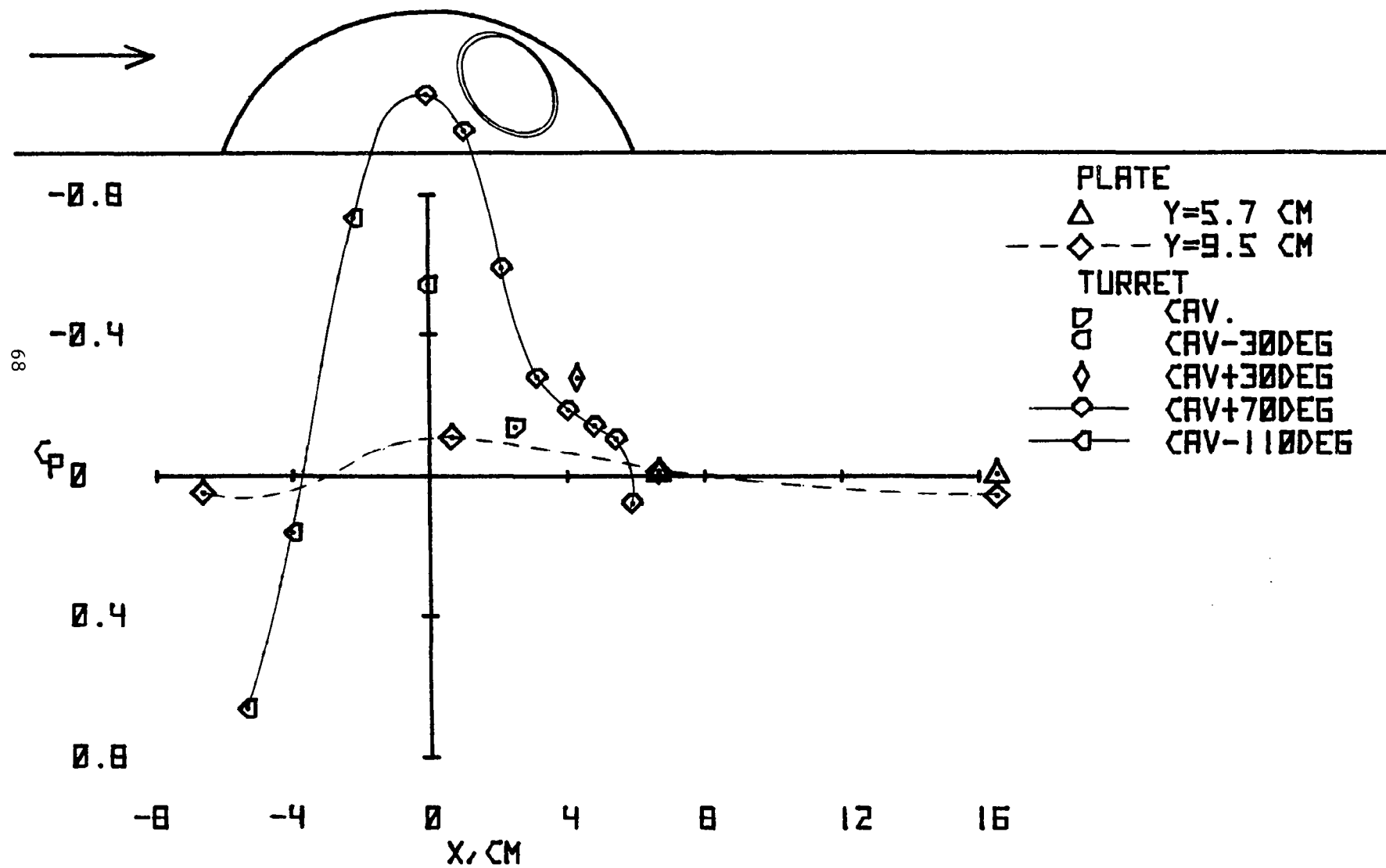
Figure 21.- Static-pressure coefficients on the turret and plate; M = 0.62, R = 5.0 million/m, θ = 120°.
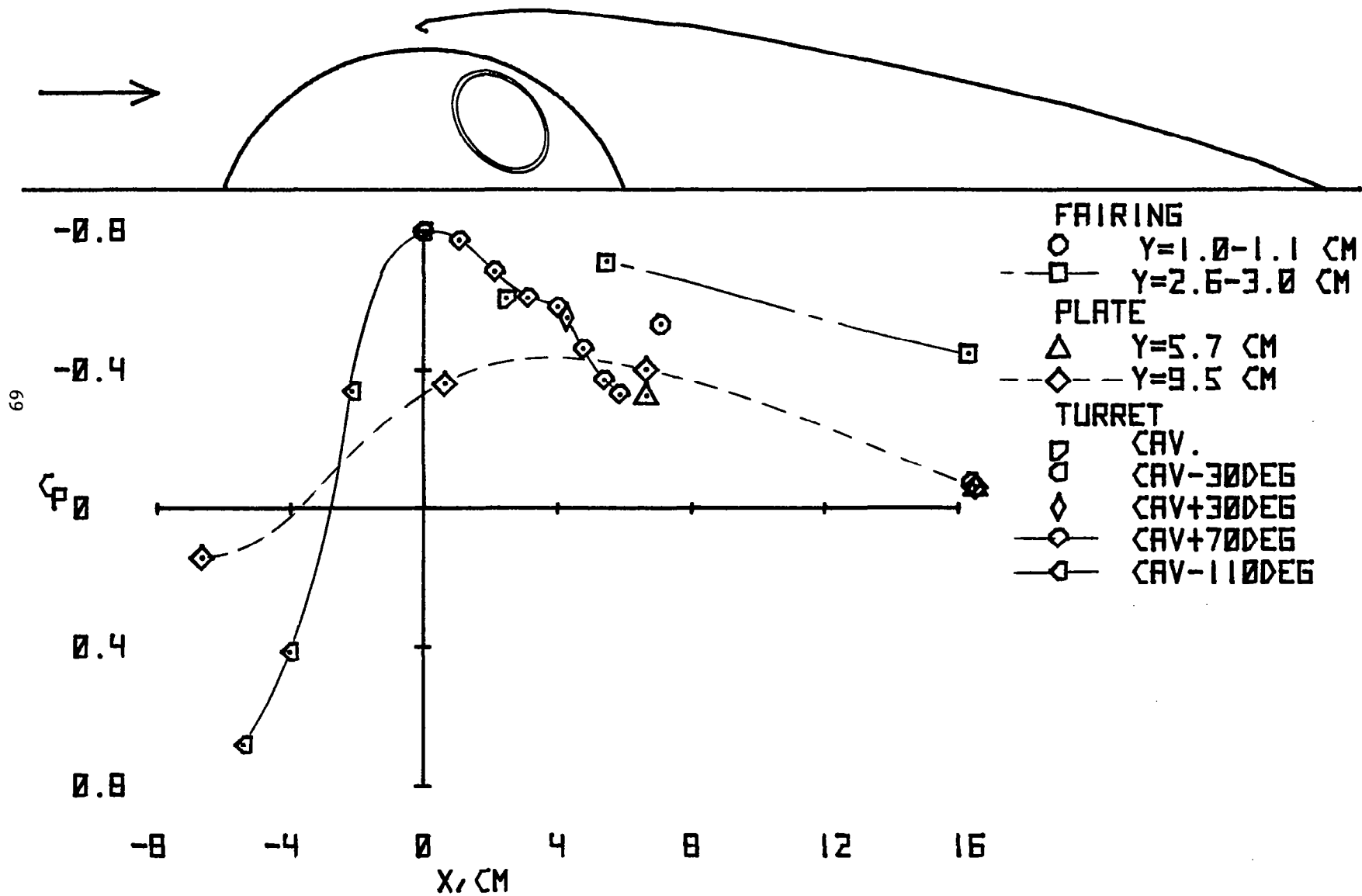
Figure 22.- Static-pressure coefficients on the turret, fairing, and plate; M = 0.95, R = 4.9 million/m, θ = 120°.
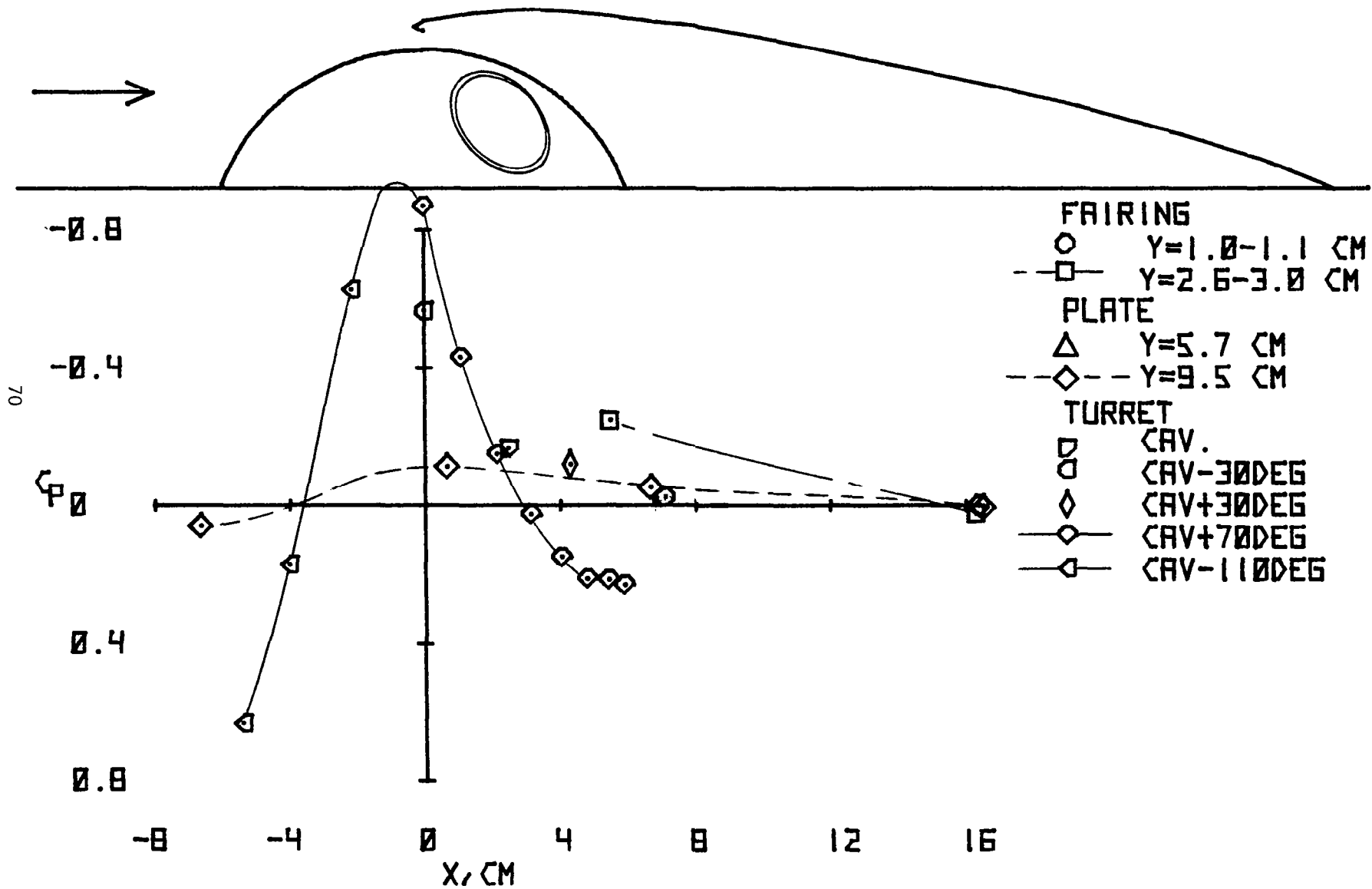
Figure 23.- Static-pressure coefficients on the turret, fairing, and plate; M = 0.62, R = 5.0 million/m, θ = 120°.
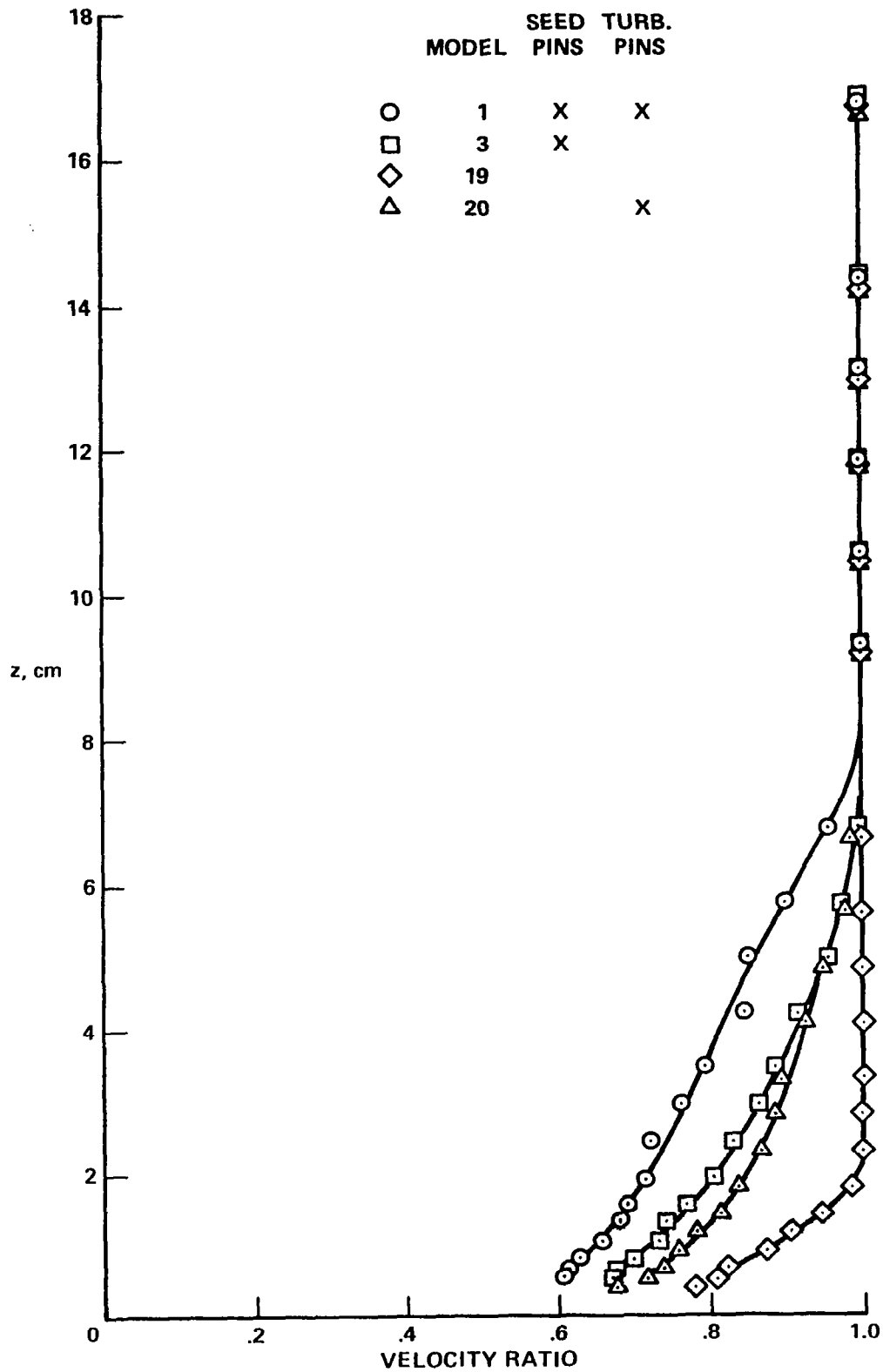
Figure 24.- Velocity profiles with and without pins; M = 0.60, R = 9.8 million/m, x = 21.6 cm, y = 0.
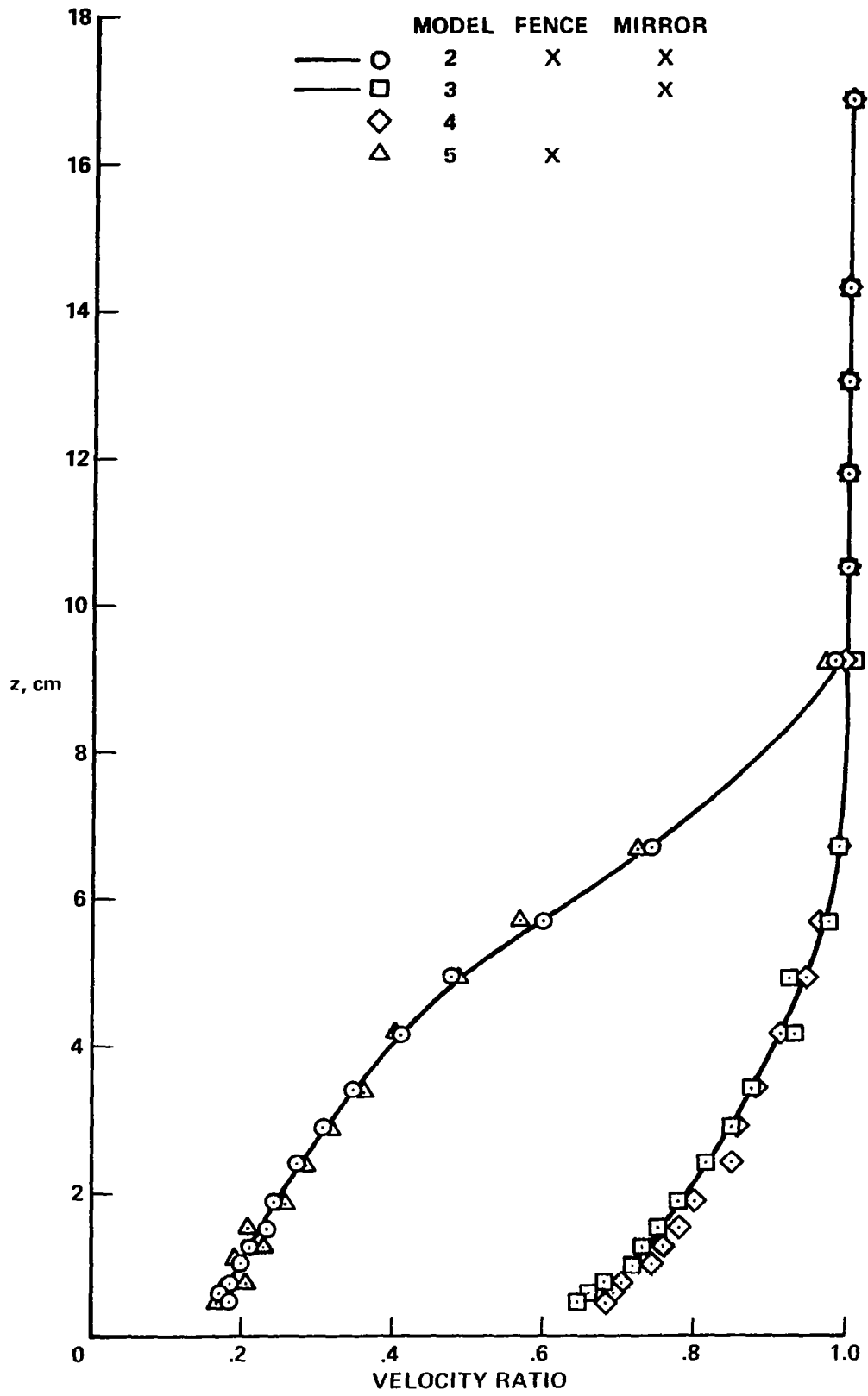
Figure 25.- Velocity profiles with and without fence and mirror; M = 0.60, R = 6.6 million/m, x = 11.4 cm, y = 0.
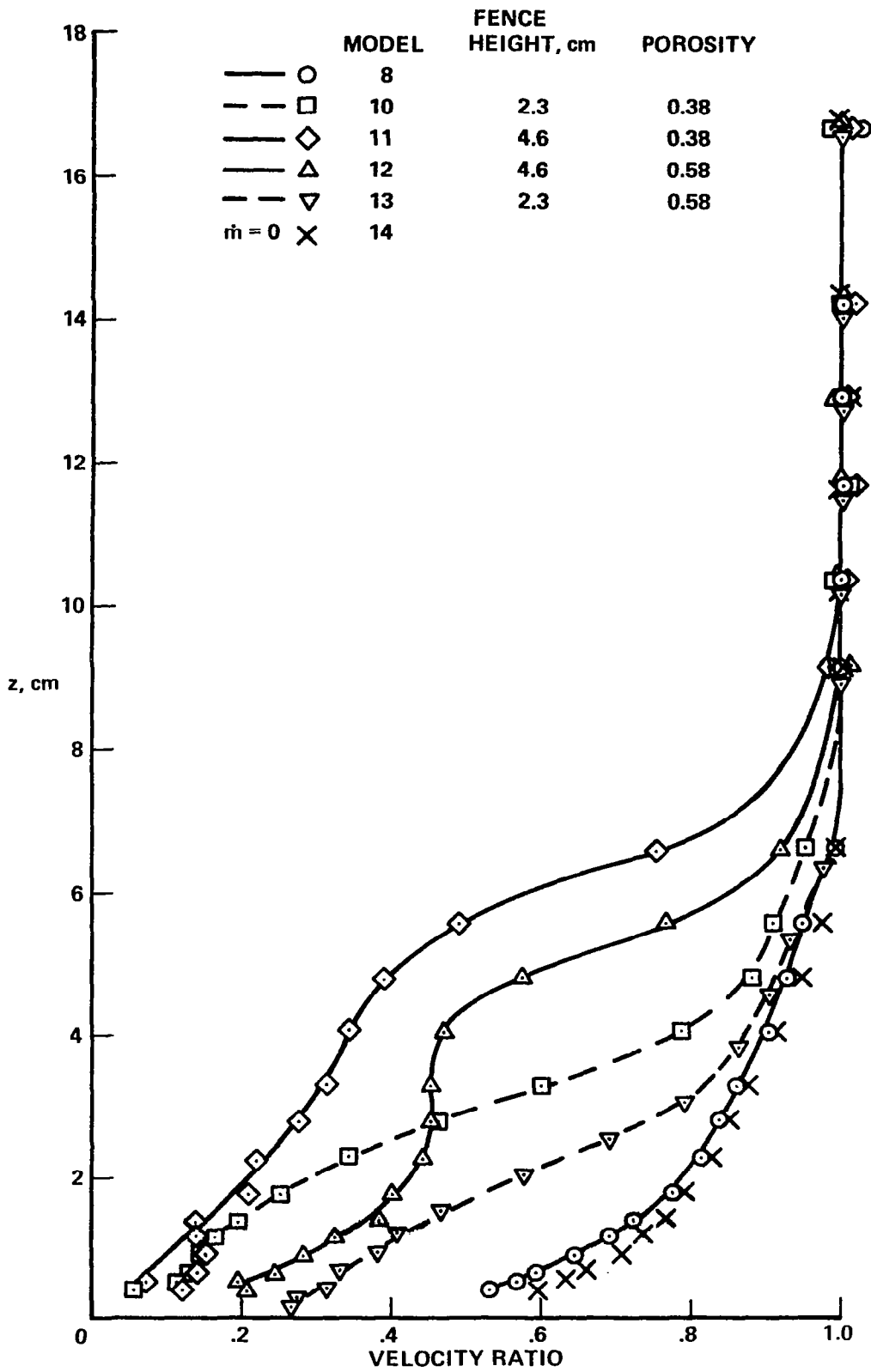
Figure 26.- Velocity profiles for cavity configurations; M = 0.60,R = 9.8 million/m, x = 7.6 cm, y = 0.1 cm.
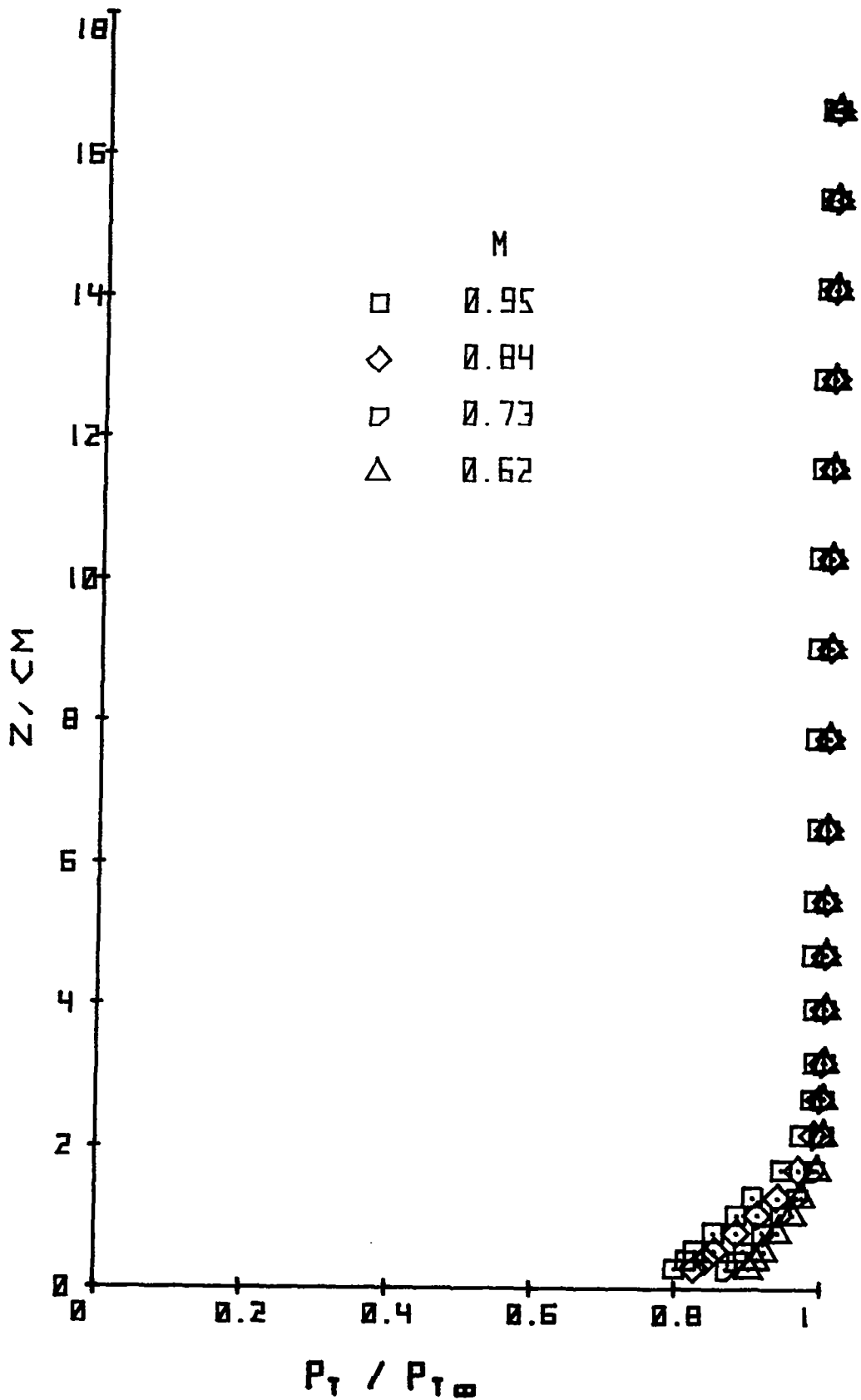
Figure 27.- Rake total pressures ahead of the turret; R = 9.9 million/m, x = -13.5 cm, y = 0, θ_{cp} = 150°.
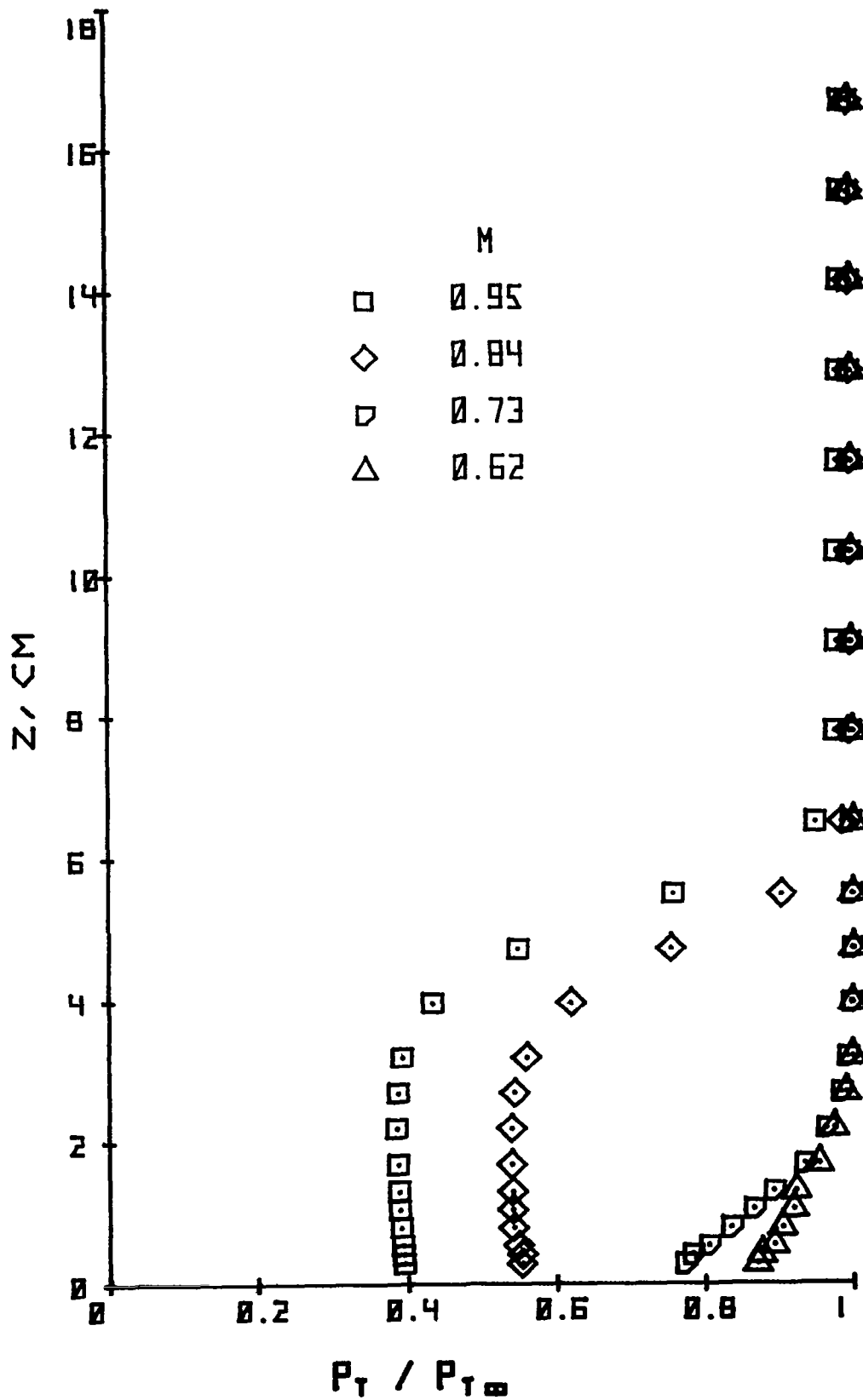
Figure 28.- Rake total pressures behind the turret; R = 9.9 million/m, x = 10.4 cm, y = 0, Θ_{cp} = 150°.

$\ominus = 150$

$\ominus = 60$

$\ominus = 90$

$\ominus = 120$
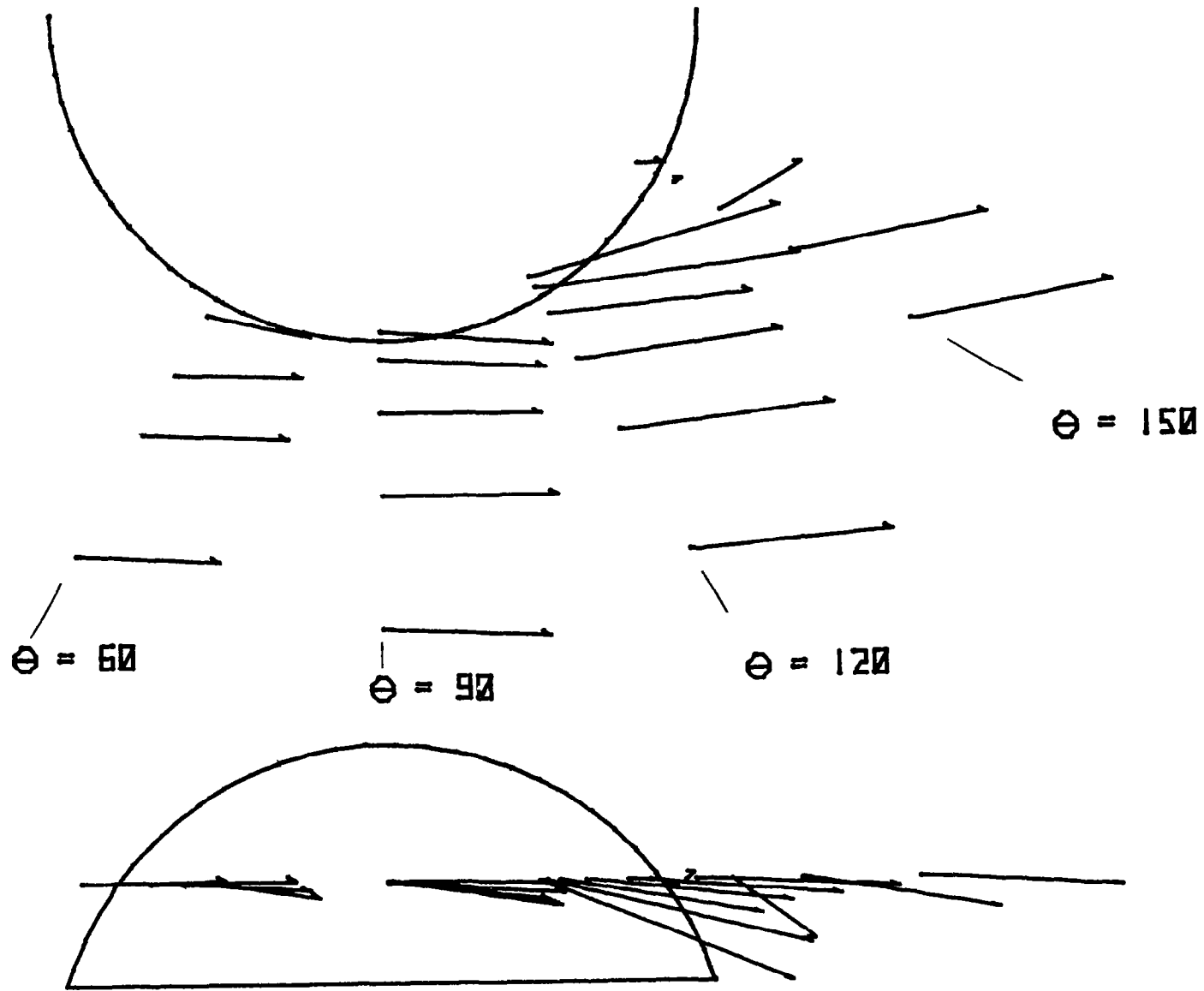
Figure 29.- Local Mach number vectors for various turret azimuths; M = 1.49, R = 4.8 million/m, z = 2.0 cm.

$\ominus$ = 150

$\ominus$ = 60

$\ominus$ = 90

$\ominus$ = 120
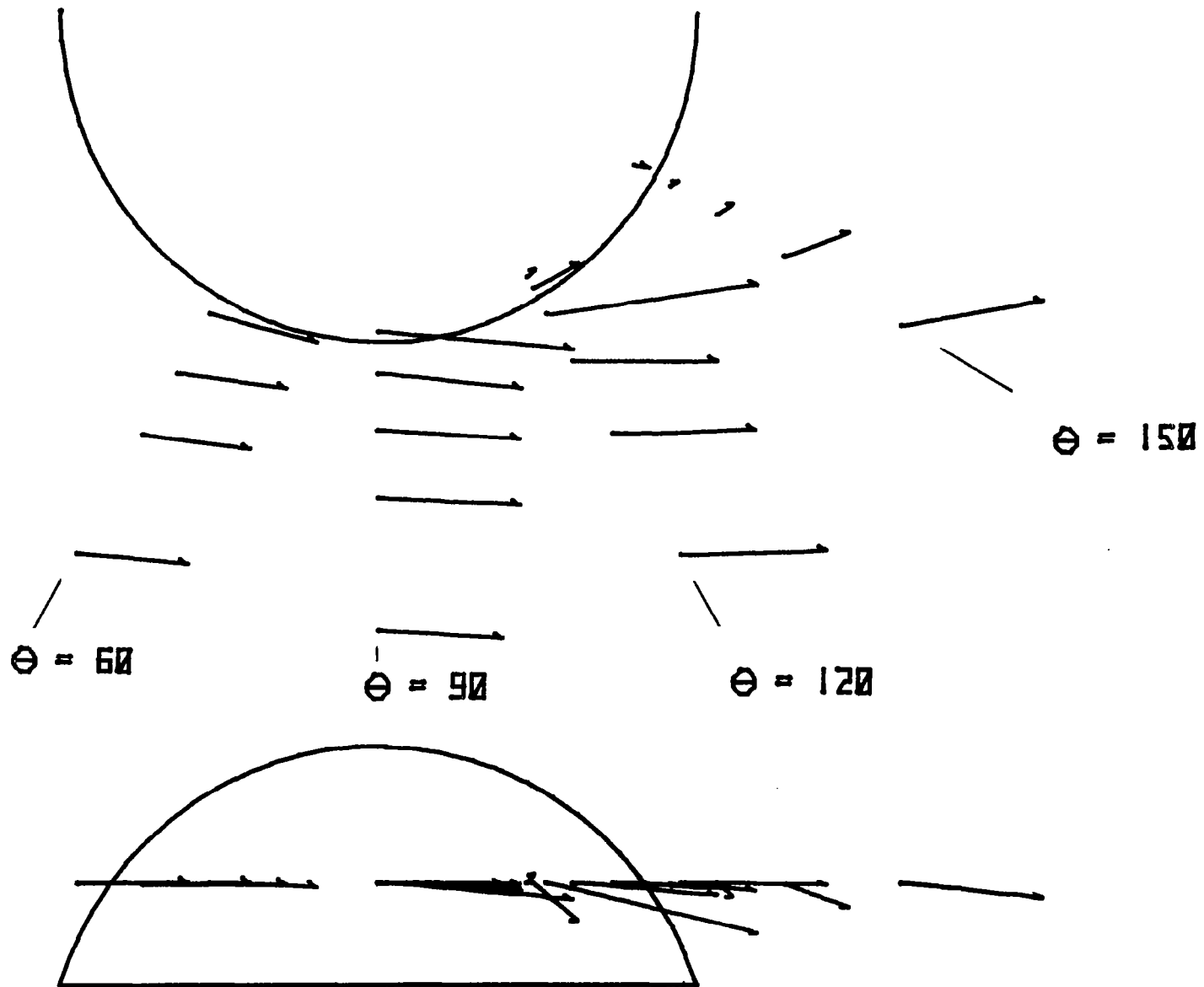
Figure 30.- Local Mach number vectors for various turret azimuths; M = 0.95, R = 4.9 million/m, z = 2.0 cm.

$\ominus = 150$

$\ominus = 60$

$\ominus = 90$

$\ominus = 120$
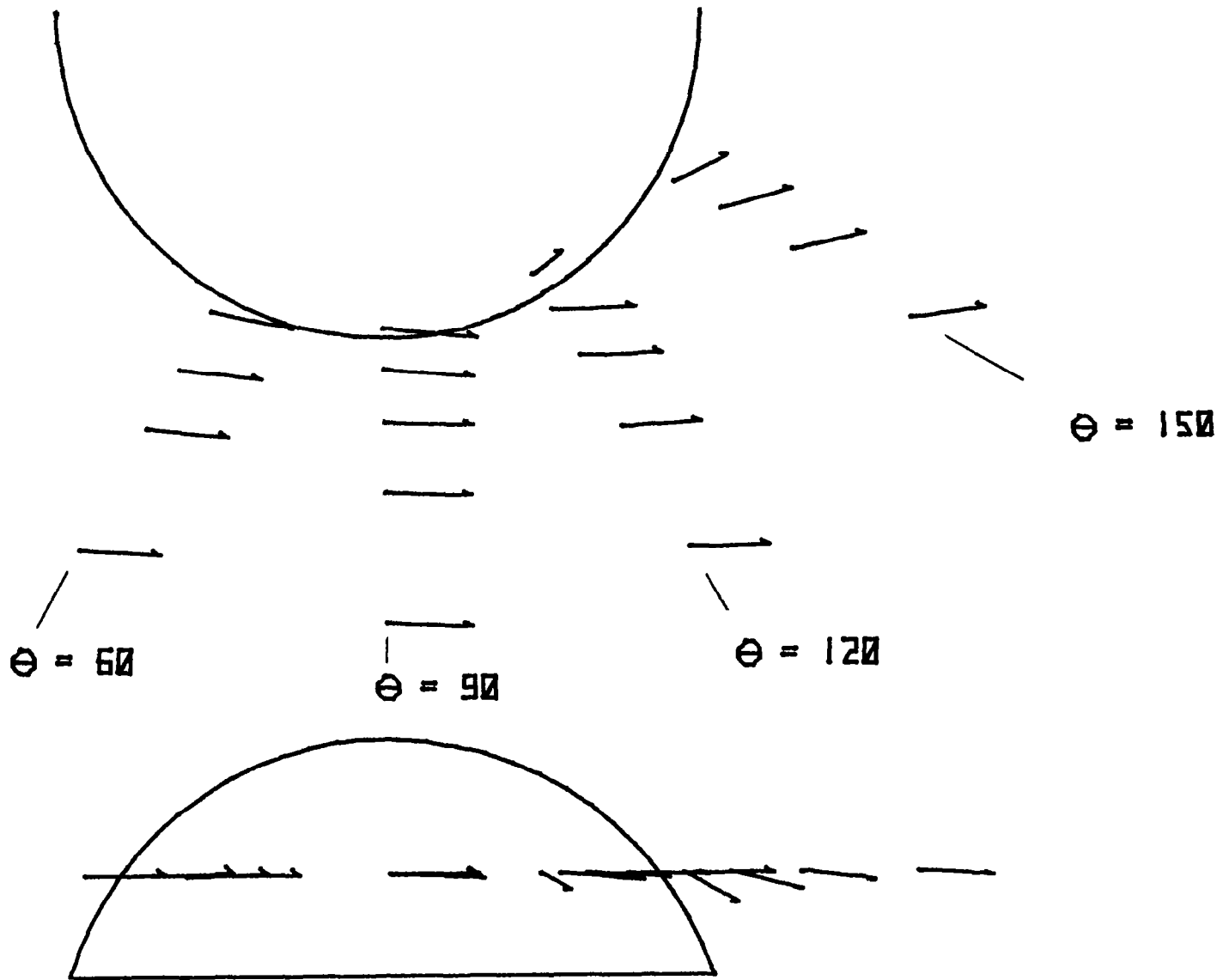
Figure 31.- Local Mach number vectors for various turret azimuths; M = 0.62, R = 5.0 million/m, z = 2.0 cm.
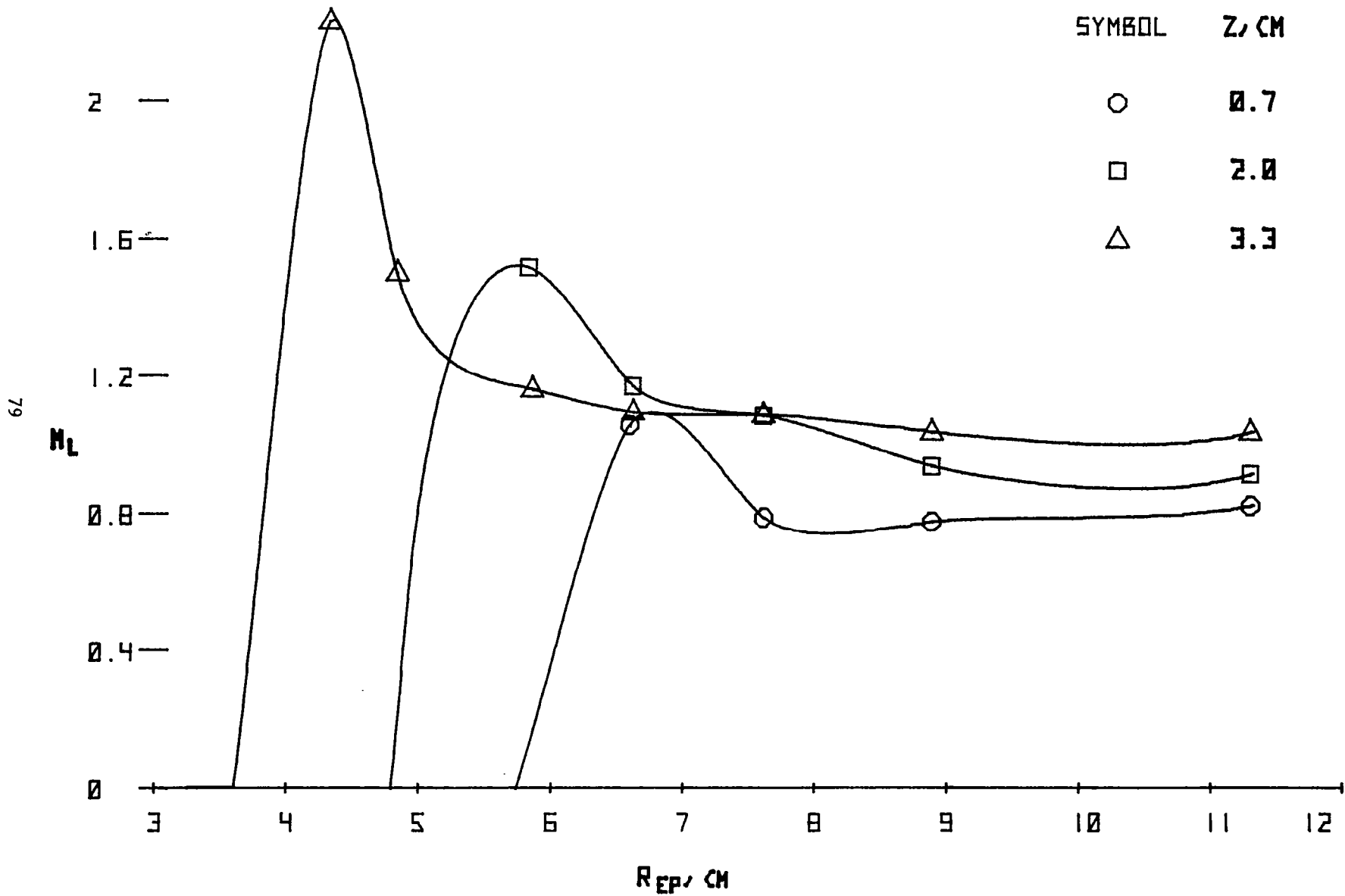
Figure 32.- Local Mach numbers along the line of sight from the turret cavity; M = 0.95, R = 9.8 million/m, θ = 90°.
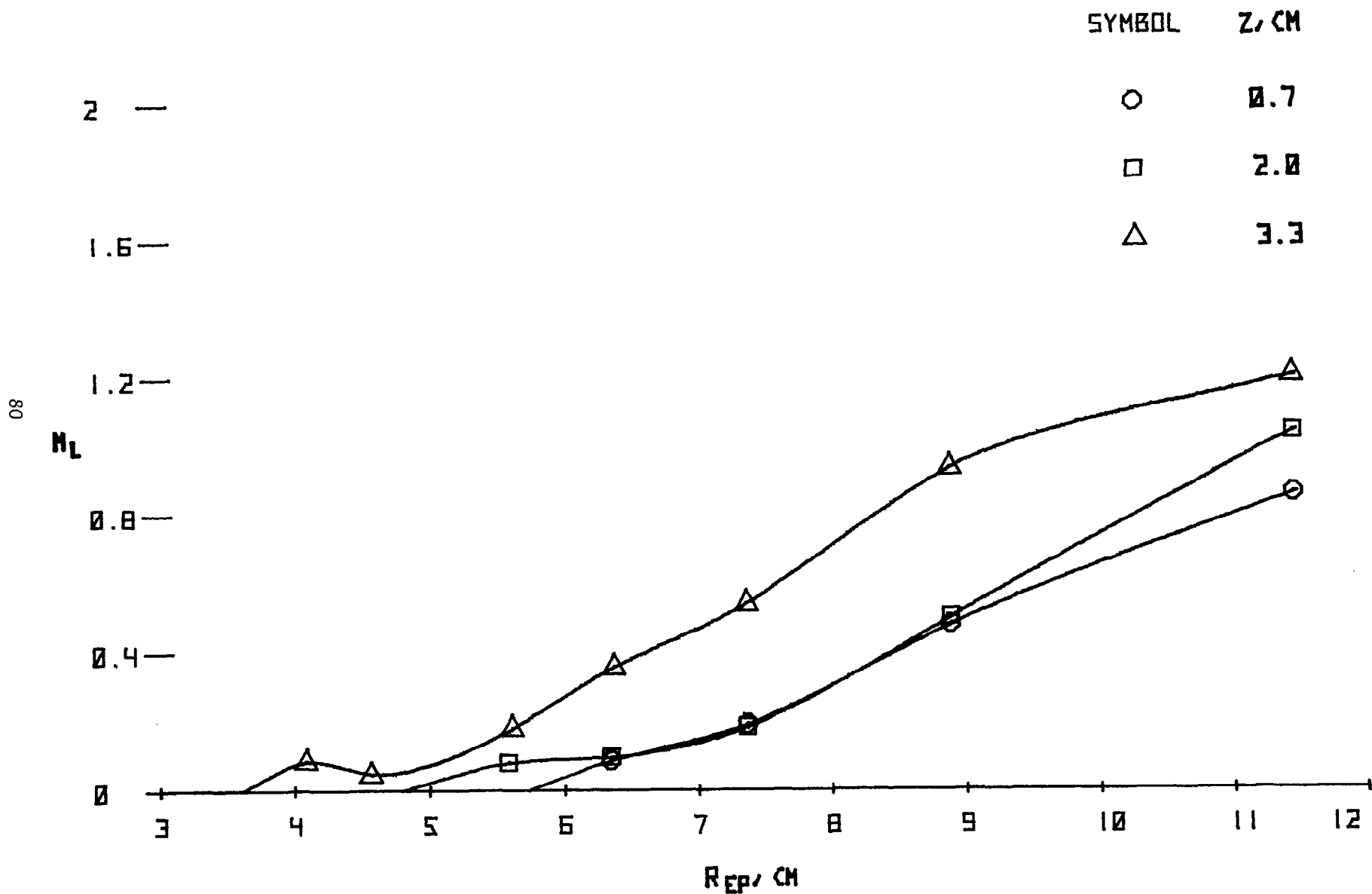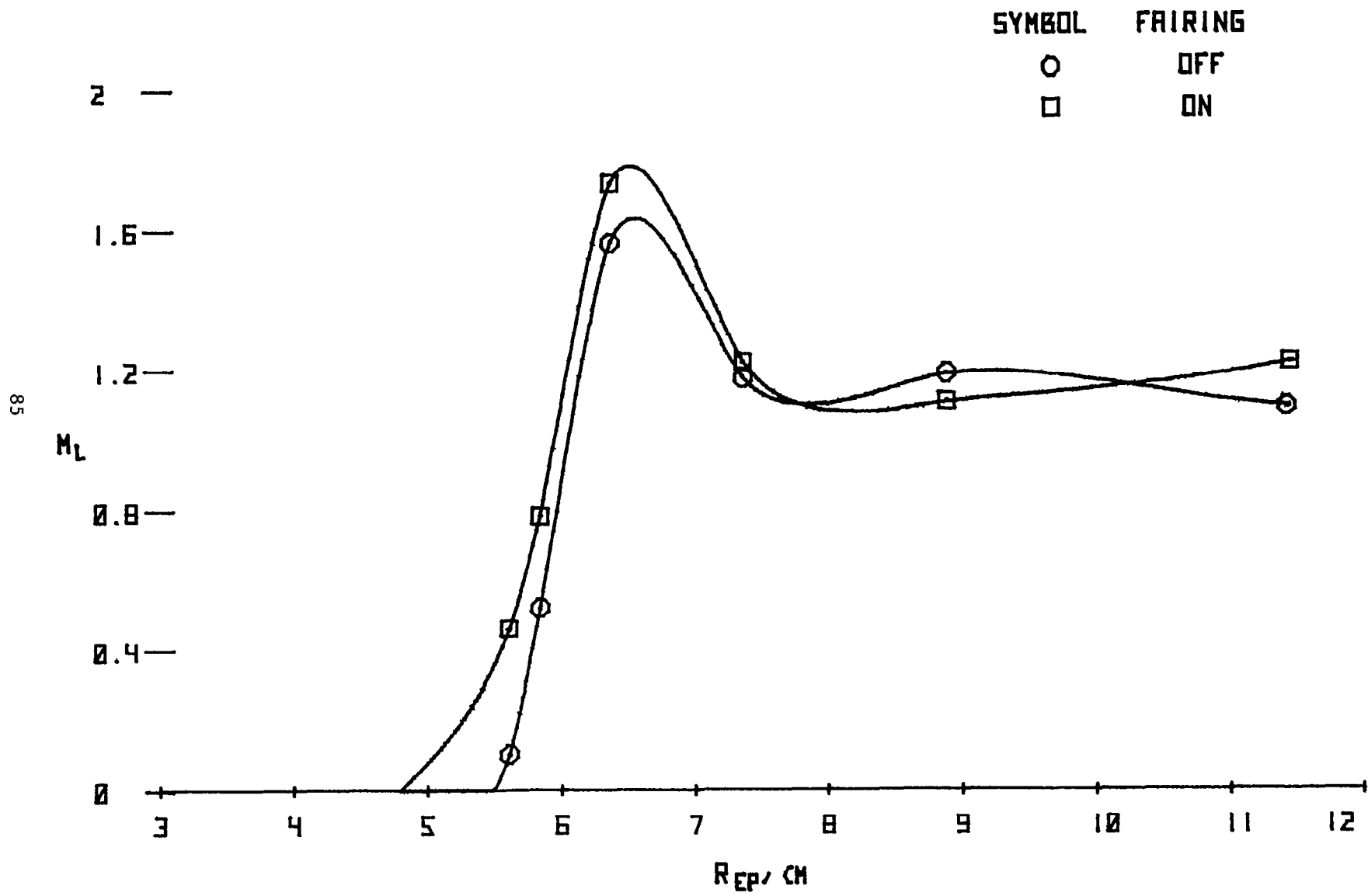
Figure 33.- Local Mach numbers along the line of sight from the turret cavity; M = 0.95, R = 9.8 million/m, $\theta = 150°$.
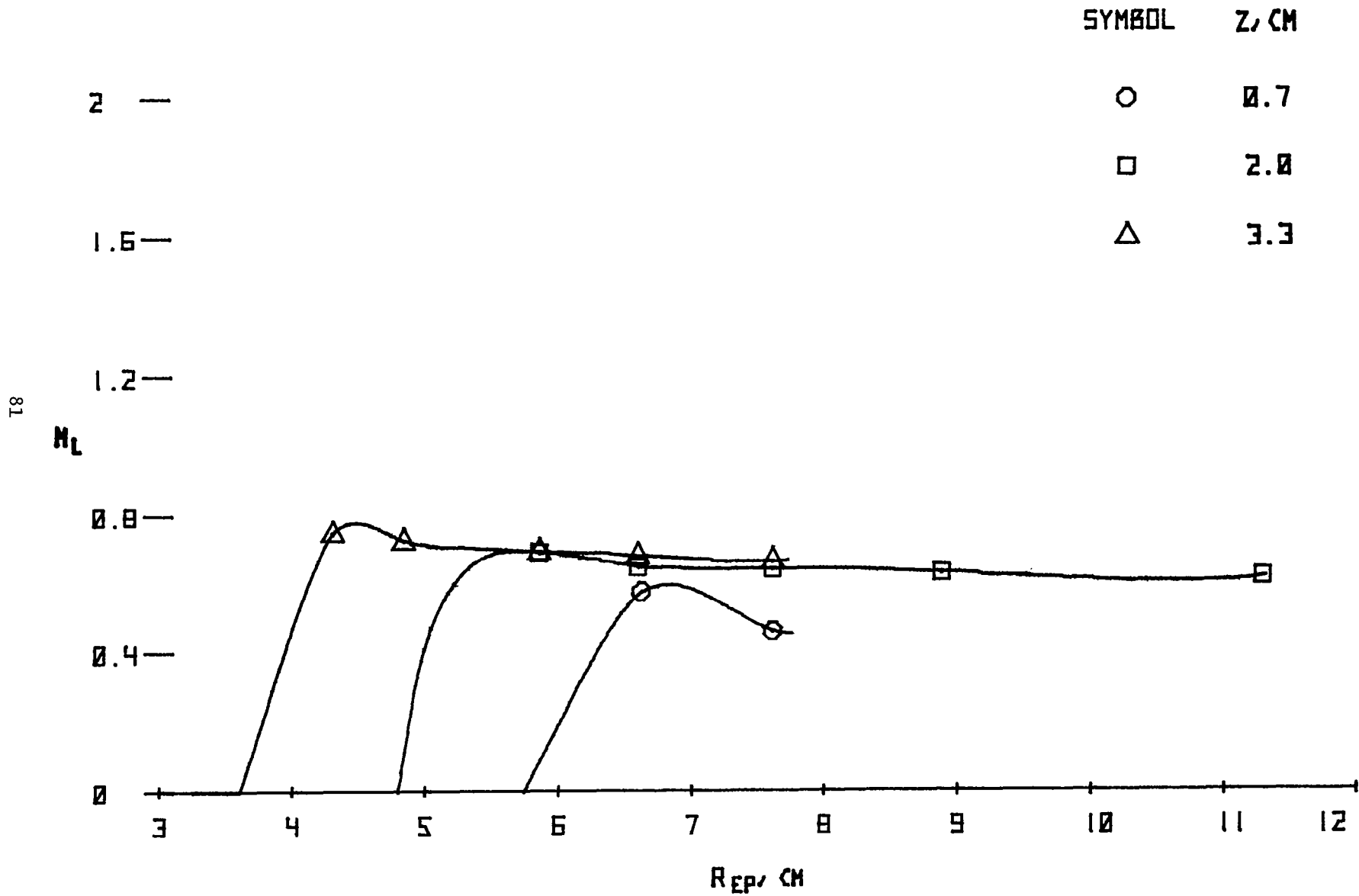
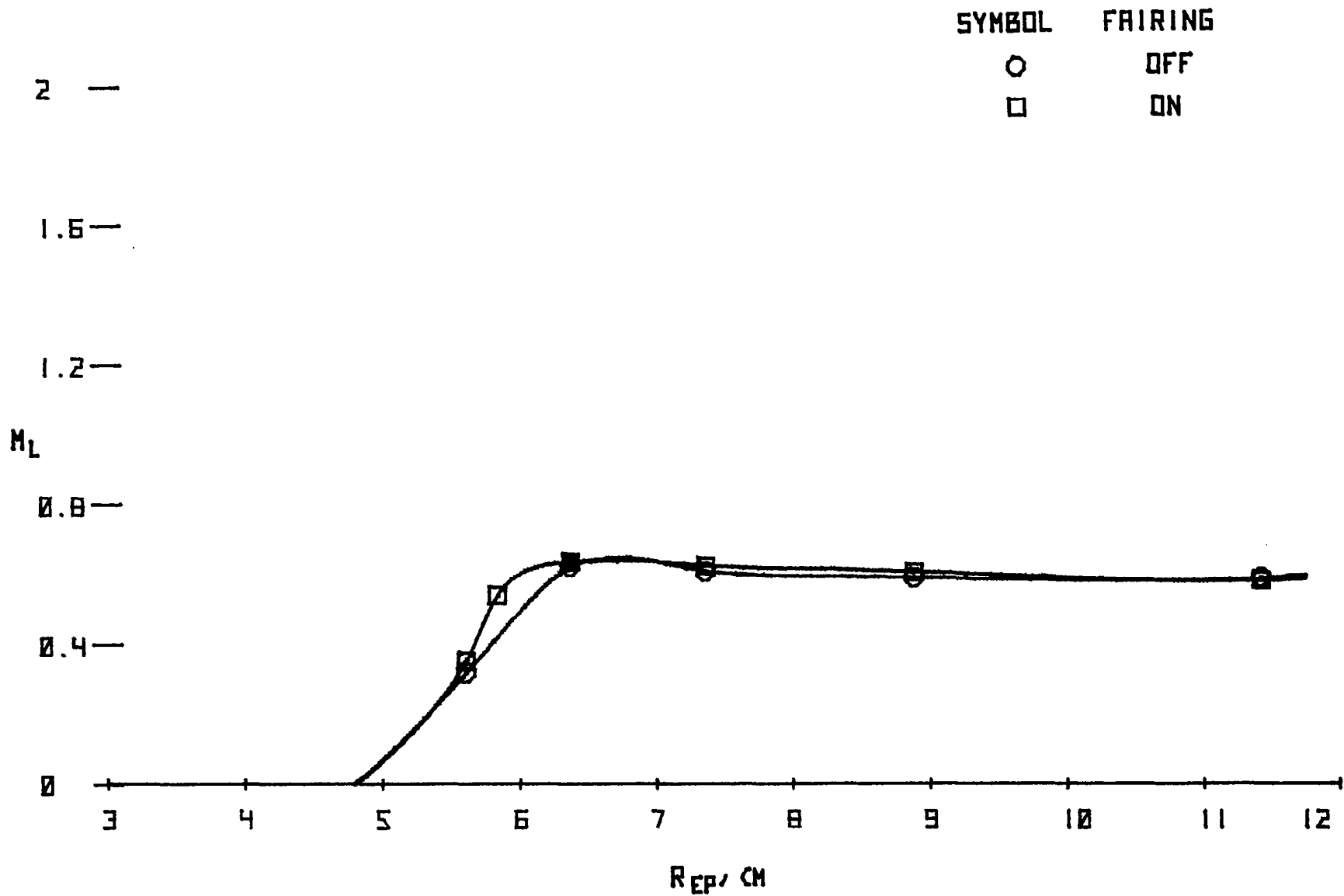Figure 34.- Local Mach numbers along the line of sight from the turret cavity; M = 0.62, R = 10.0 million/m, θ = 90°.
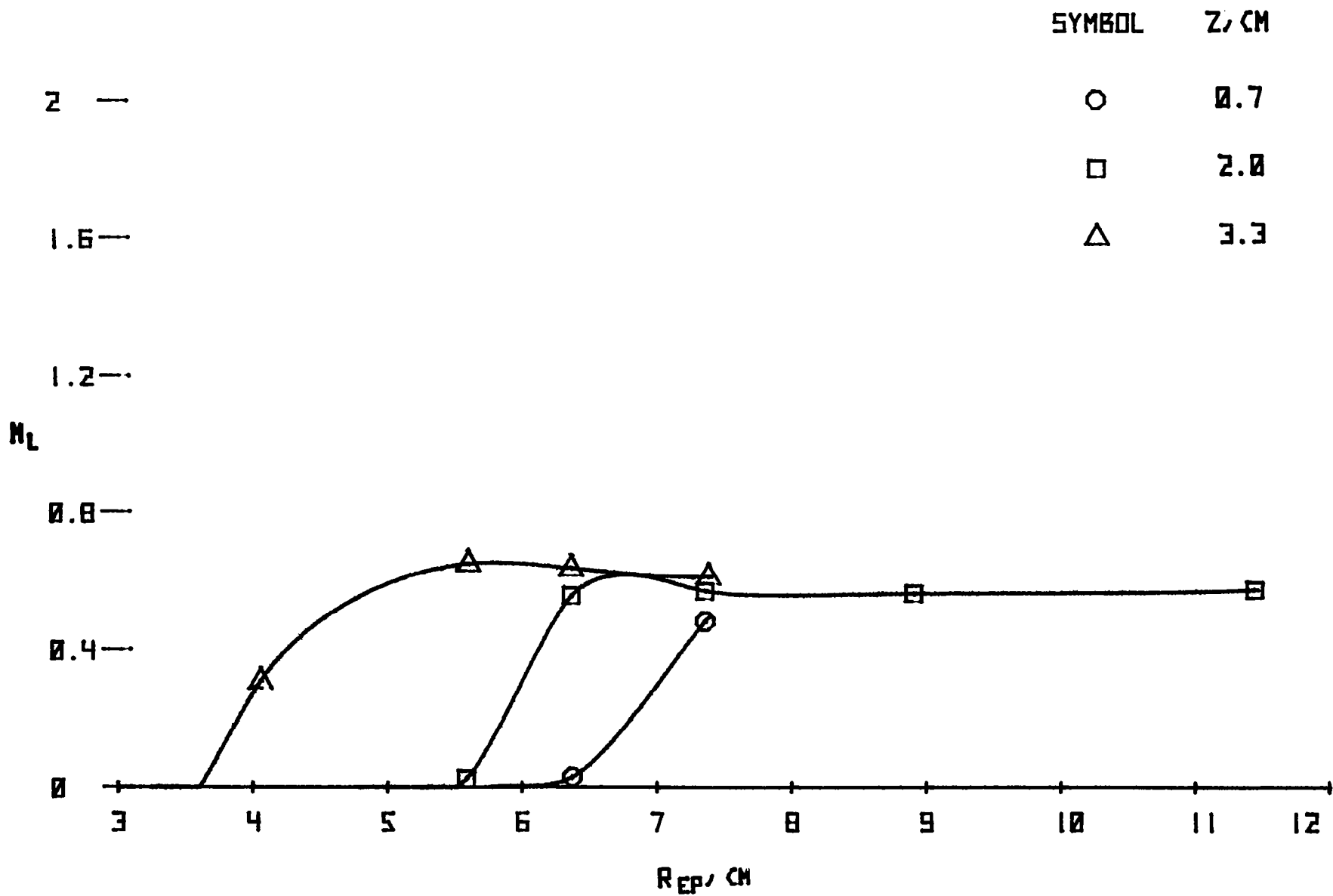
Figure 35.- Local Mach numbers along the line of sight from the turret cavity; M = 0.62, R = 10.0 million/m, $\theta = 150^\circ$.

82
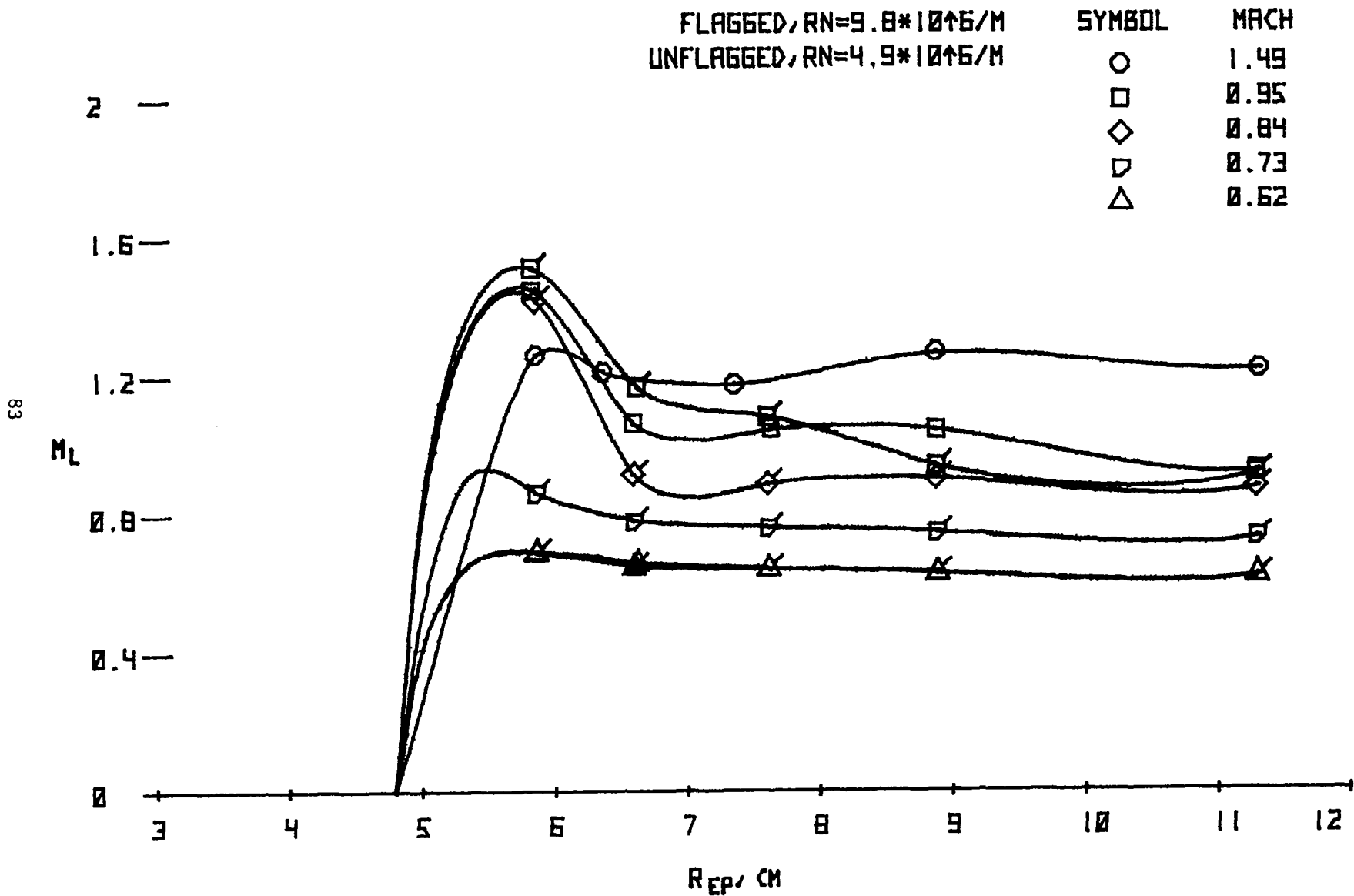
Figure 36.- Local Mach numbers along the line of sight from the turret cavity; $\theta = 90^{\circ}$, z = 2.0 cm.
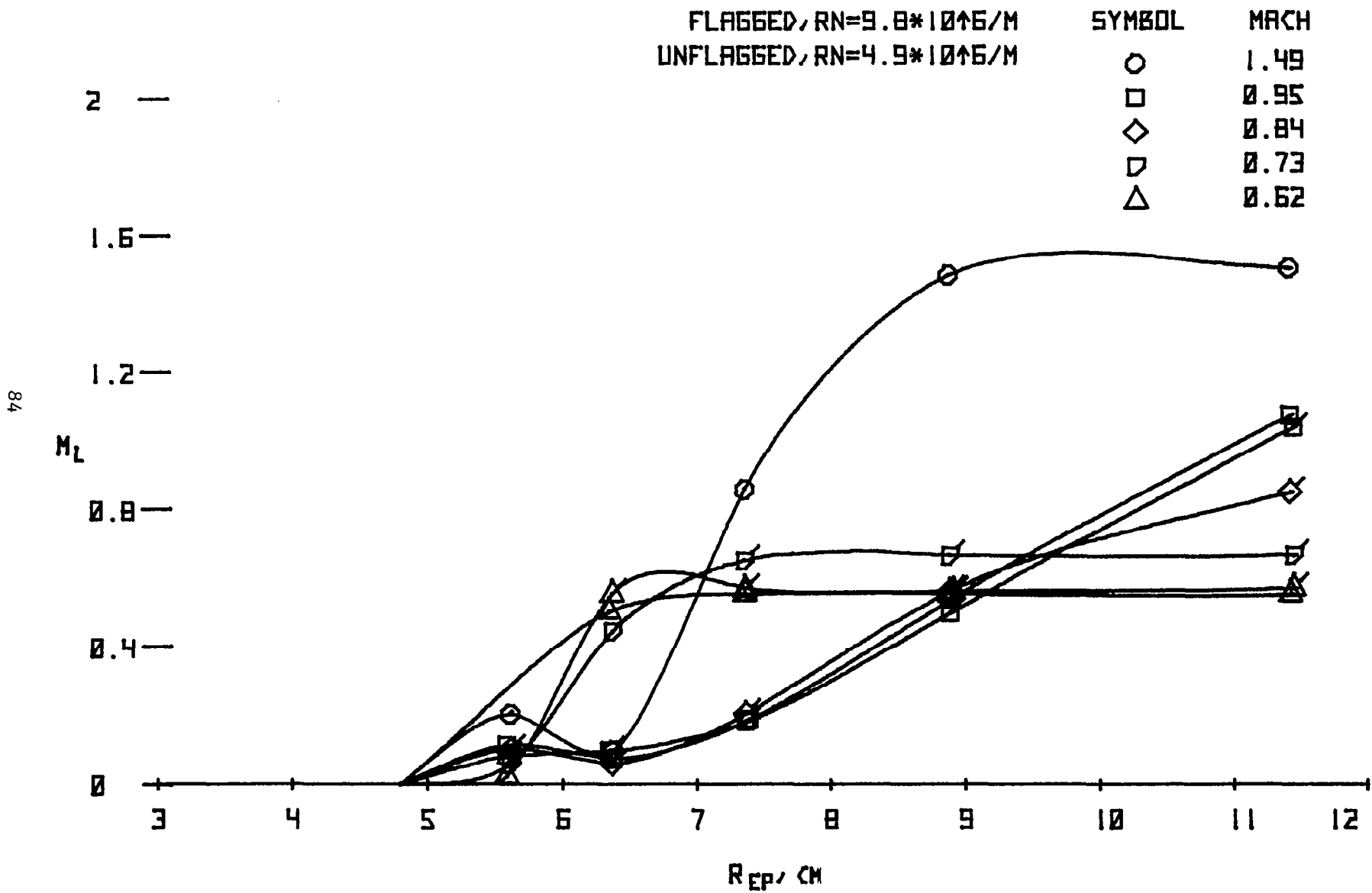
Figure 37.- Local Mach numbers along the line of sight from the turret cavity; θ = 150°, z = 2.0 cm.

84

Figure 38.- Local Mach numbers along the line of sight from the turret cavity; M = 0.95, R = 9.8 million/m, θ = 120°, z = 2.0 cm.

Figure 39.- Local Mach numbers along the line of sight from the turret cavity; M = 0.62, R = 10.0 million/m, θ = 120°, z = 2.0 cm.
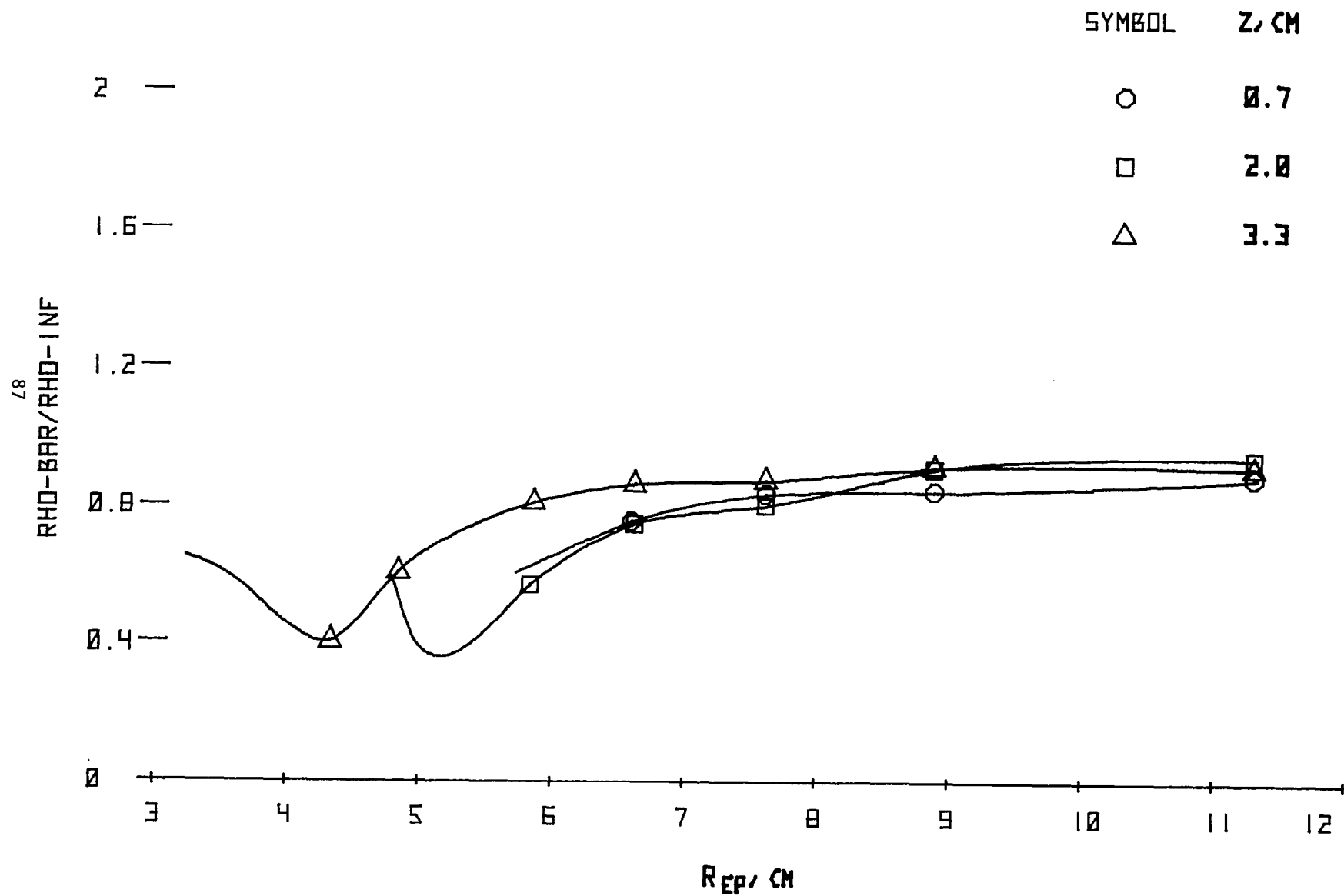
Figure 40.— Local density along the line of sight from the turret cavity; M = 0.95, R = 9.8 million/m, Θ = 90°.
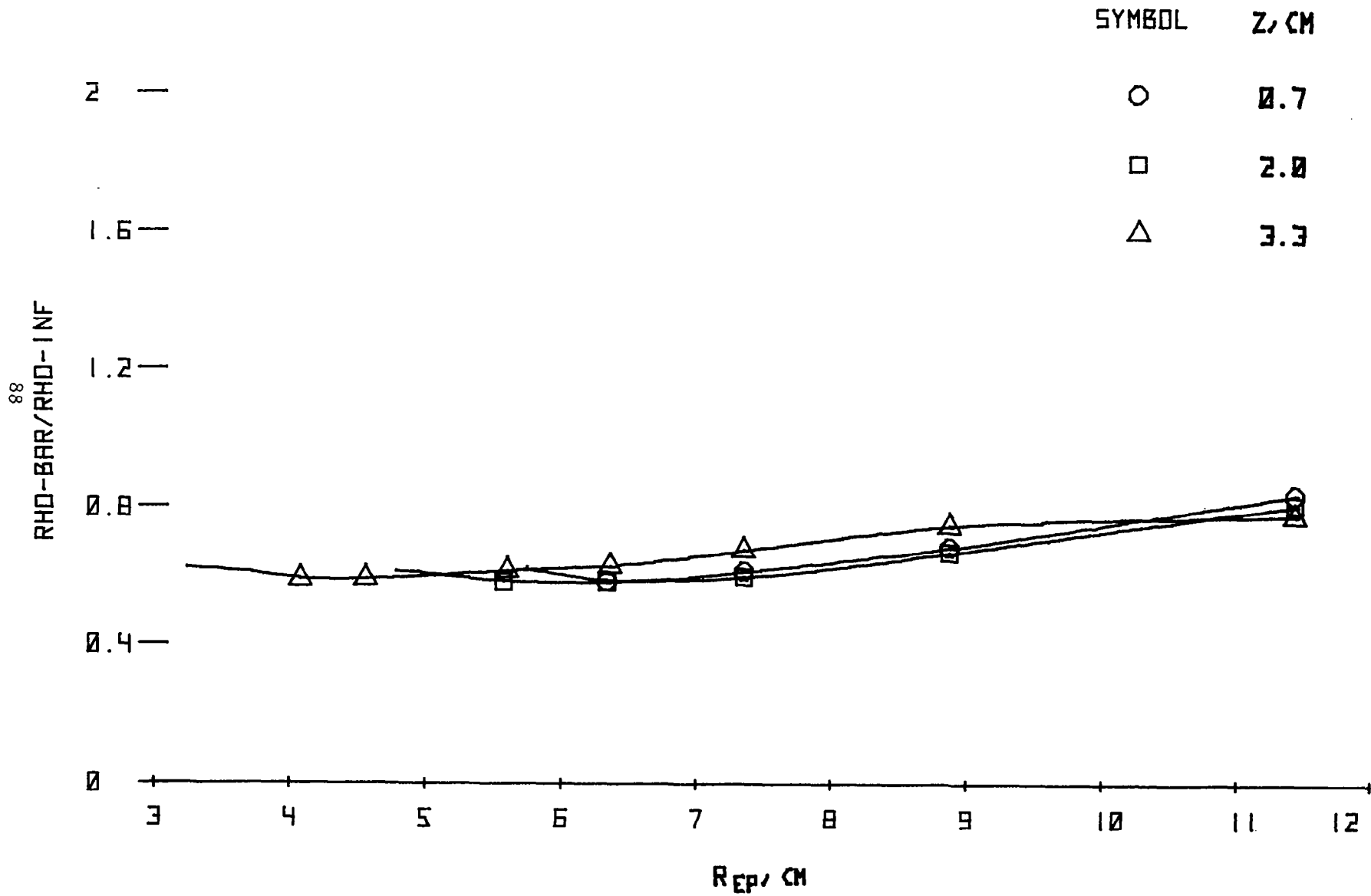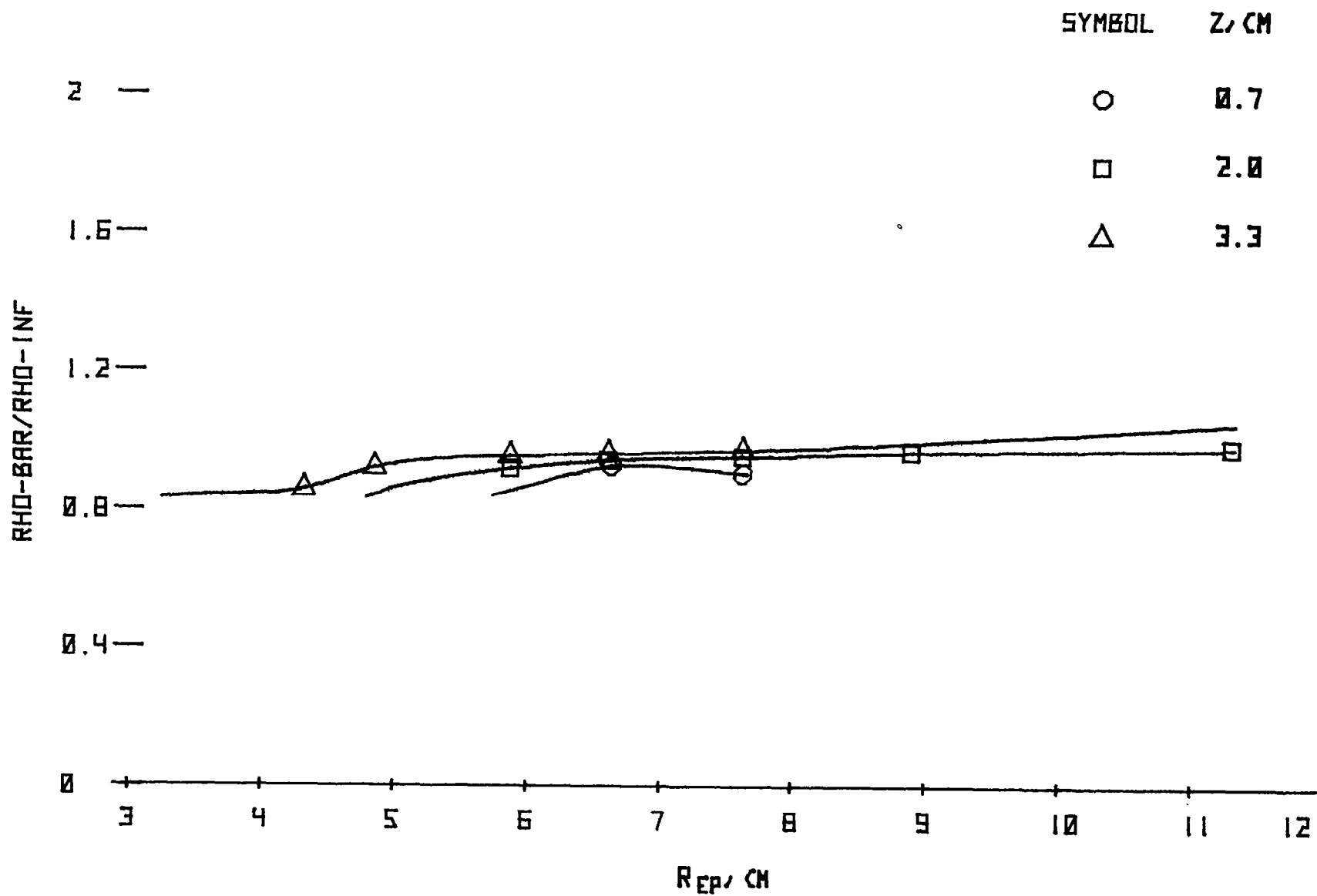
Figure 41.- Local density along the line of sight from the turret cavity; M = 0.95, R = 9.8 million/m, θ = 150°.

Figure 42.- Local density along the line of sight from the turret cavity; M = 0.62, R = 10.0 million/m, θ = 90°.

SYMBOL   Z, CM

○   0.7

□   2.0

△   3.3

2 —

1.6—

1.2—

RHO-BAR/RHO-INF

0.8—

0.4—·

0

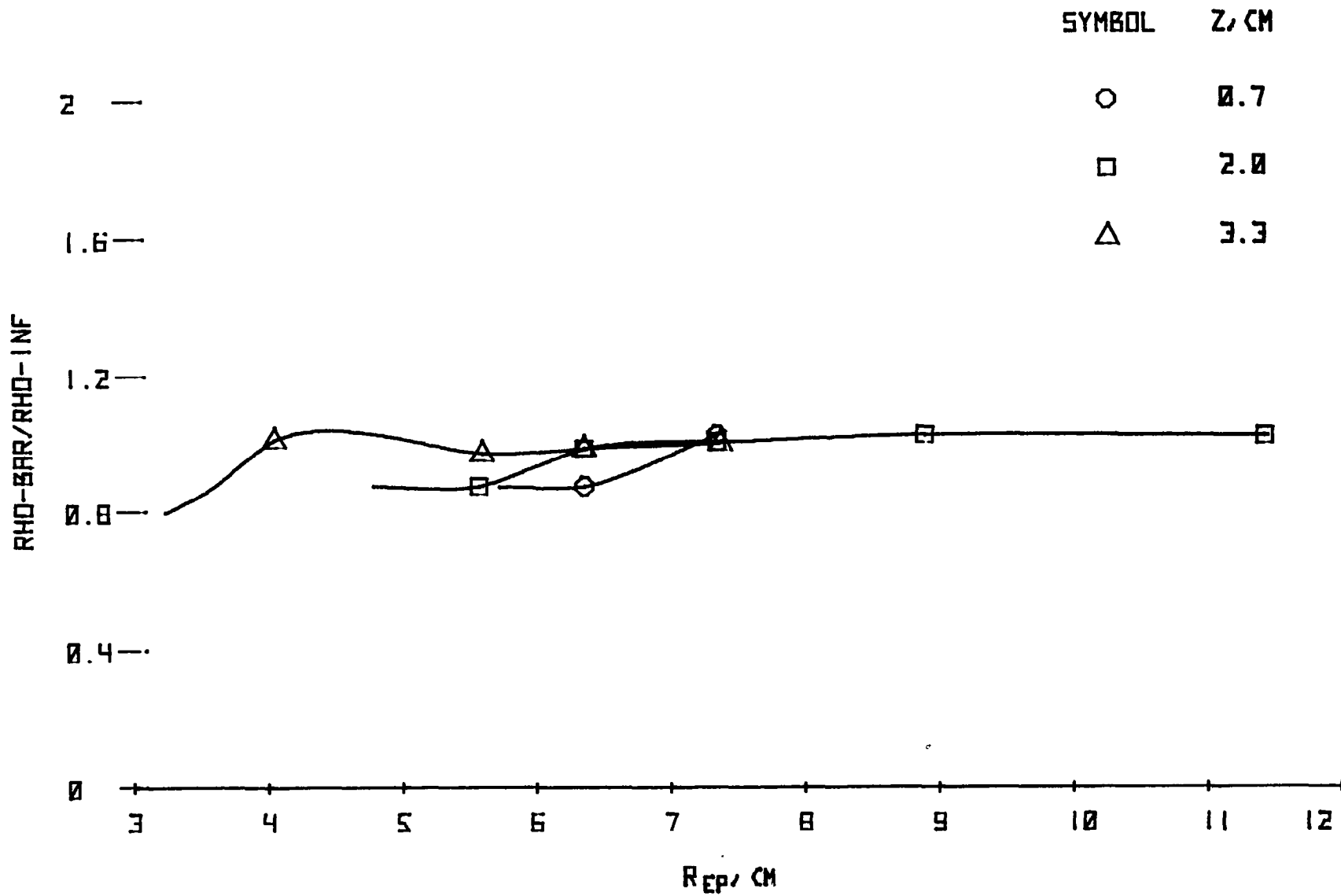3   4   5   6   7   8   9   10   11   12

R$_{EP}$, CM

Figure 43.- Local density along the line of sight from the turret cavity; M = 0.62, R = 10.0 million/m, $\Theta = 150^{\circ}$.